UNIVERSITY OF THESSALY

POLYTECHNIC SCHOOL

DEPARTMENT OF MECHANICAL ENGINEERING

LABORATORY OF MATERIALS

Diploma Thesis

"Corrosion-induced hydrogen absorption and the effect of aging treatment in Aluminum alloy 2024"

By

Thanasis C. Kefalas

Thesis supervisor:

Dr. Eleni Kamoutsi

Submitted in partial fulfillment of the requirements for the Mechanical Engineering Diploma from University of Thessaly.

Volos, February 2020

Certified by the members of the Thesis Committee:

First Examiner (Supervisor)	Dr. Helen Kamoutsi Lab Teaching Staff, Department of Mechanical Engineering, University of Thessaly
Second Examiner	Dr. Vasilis Bontozoglou Professor, Department of Mechanical Engineering, University of Thessaly
Third Examiner	Dr. Alexis Kermanidis Associate Professor, Department of Mechanical Engineering, University of Thessaly

Contents

Table of Figures

Table of Tables

Acknowledgments

In writing my diploma thesis, I would like to express my great gratitude to Mrs. Helen Kamoutsi for her patience and generous help, Mr. Gregory Haidemenopoulos because he was the one who inspired me to deal with this field and last but not least my family and my friends who supported me all those years.

Chapter 1 -Introduction

1.1Description of the problem

Corrosion presents a major concern to the structural integrity of aging aircraft structures. As the time of an aircraft structure in service increases, there is a growing probability that corrosion will interact with other forms of damage, such as single fatigue cracks or multiple-site damage in the form of widespread cracking at regions of high-stress gradients; it can result in loss of structural integrity and may lead to fatal consequences. Thus, the effect of corrosion on the damage tolerance ability of advanced aluminum alloys calls for a very diligent consideration of the problems associated with the combined effect of corrosion and embrittling mechanisms. Recently there has been an increased attention in basic research and development concerning structural integrity, taking into account the related corrosion aspects [1-3]. It has been realized that the establishment of damage functions for quantifying the simultaneous accumulation of corrosion and fatigue-induced damage is very complex and demanding. Therefore, despite the advancements in modeling fatigue crack growth [4-7] and multiple-site damage phenomena [1-3], the assessment of structural degradation in aging aircraft is still relying heavily on test data. To face the corrosion- induced structural degradation issue, available data usually refer to accelerated laboratory corrosion tests and, more rarely, to in-nature atmospheric or marine exposure corrosion tests.

With the exception of the atmospheric corrosion test where, according to the relevant specification the tensile properties of corroded specimens are measured as well, these tests are used for evaluating the corrosion susceptibility of the materials by measuring weight loss and characterizing depth and type of corrosion attack. The above methodology towards understanding corrosion susceptibility of a material does not relate corrosion to it's immediate effect on the material's mechanical behavior and residual properties. Yet, it is exactly these missing data that are needed to face structural integrity problems of corroded aircraft components. Corrosion-induced mechanical degradation studies have been based mainly on the results of stress corrosion cracking tests [8, 9] or, more rarely on the results of fatigue tests performed in the presence of a corrosive environment [1-3]. Both types of tests provide useful results; they refer, however, to the case where a material is loaded in a corrosive environment but not to situations where a corroded material is subjected to mechanical loads. Present-day considerations on corrosion-induced structural degradation associate the presence of corrosion with a decrease in the load-bearing capacity of the corroded structural member [2, 10].

What is more, this decrease is associated with the presence of corrosion notches that lead to local increase of stress promoting fatigue crack initiation as well. In addition, corrosion-induced reduction of the members' load-bearing thickness which, in the case of the thin alloy skin sheets may be essential, can lead to appreciable increase of stress gradients [10].The above consideration of the corrosion-induced structural integrity issue is consistent with the classical understanding of the corrosion attack of aluminum alloys as the result of complex oxidation processes at the materials surface.

The aforementioned considerations gain particular importance if the so-called "aging aircraft" issue is considered. The aging aircraft has accumulated corrosion damage over the service life and its residual life depends on possible degradation stemming from corrosion-induced embrittling mechanisms. One typical example where failure was attributed to corrosion-induced multi-site damage (MSD) has been the Aloha Airlines accident in 1988. The Figure insert shows the possible mechanism of damage, i.e. growth and linkage of multiple fatigue cracks, emanating from rivet holes. Recent investigations in the Hellenic Aerospace Industry (HAI) on firefighting planes have shown considerable corrosion damage around rivet holes.

There are three key questions regarding this issue:

1. Is there a corrosion-induced degradation of ductility, which in turn degrades damage tolerance and the residual life of aerostructures?

2. What is the underlying corrosion-induced embrittling mechanism?

3. What is the effect of the microstructural characteristics of the material on hydrogen trapping?

The answer to the first question has been provided by a long series of experiments, conducted at the University of Patras [11, 12], on mechanical testing of pre-corroded (in EXCO) alloy 2024. It was shown that (i) degradation of ductility increases with corrosion exposure time and (ii) removal of the corrosion layer restores strength but not ductility. These results indicated the operation of a bulk corrosion-induced embrittlement mechanism. The second question was answered by previous work performed in the Laboratory of Materials in the Department of Mechanical Engineering in Volos, Greece . Hydrogen is produced by surface corrosion reactions and a significant part of it is absorbed in atomic form into the material [11]. In particular, the production of atomic hydrogen by a single-electron transfer process according to the reaction:

makes water an aggressive environment for aluminum alloys [9]. Absorbed hydrogen diffuses towards the interior of the material and may be retained at various preferential locations [13-15]. More specifically, it is being trapped in distinct energy states, which correspond to different microstructural traps. These traps are then activated and release hydrogen at different temperatures. In alloy 2024, four traps T1 to T4 were identified. Trap T1 is considered as a reversible trap, which releases hydrogen continuously at low temperatures. Traps T2, T3 and T4 saturate with exposure time and are considered to be irreversible. The hydrogen front advances with the corrosion front, so hydrogen penetrates deep in the material through the intergranular paths generated by the corrosion process. Then, hydrogen diffuses further in the material establishing a hydrogen-affected zone beneath the corrosion depth of attack.

Different microstructures were produced in alloy 2024 by differentiating the heat treatment conditions of artificial aging. Peak and overaged conditions were achieved by heat treatments for aging temperatures of 210°C and 170°C, for extended duration, up to 98h. The present investigation has been conducted in an attempt to get a better insight of the trapping of hydrogen in aluminum alloy 2024. The series of specimens were artificially aged at temperatures range of 150 to 160 °C from 0,5 to 264h. To that end, the experiments were designed to alter the materials microstructure prior to corrosion exposure and associated hydrogen uptake. The present work focuses on the effect of aging on corrosion-induced hydrogen trapping of Al alloy 2024 and attempts to answer the key question on how the microstructural characteristics of the alloy interact with the produced hydrogen.

Thesis objectives

In view of the above considerations, the present thesis attempts to further elucidate the effect of the microstructural characteristics of the material on hydrogen trapping.

Therefore, the main objectives of this thesis are the following:

1) To establish a correlation, if any, between corrosion and precipitate population.
2) To establish a correlation, if any, between precipitate population and hydrogen trapping/uptake.

Thesis methodology

Research was focused on aircraft aluminum alloy 2024 in the T351 temper. The experimental procedures involved the following actions:

(1)Heat treatments,

(2)Accelerated corrosion testing (using the EXCO test environment),

(3)Detailed microstructural investigation of the evolution of corrosion damage by employing metallography

(4)Hydrogen measurements by employing an in-house thermal desorption spectroscopy / gas chromatography system (TDS)

Thesis outline

The thesis outline is as follows

Chapter2 - Literature review

Chapter3 - Experimental procedures

Chapter 4 - Results and Discussion

Chapter 5 - Conclusions

Chapter 6 - Proposed Future Work

Chapter 2 - Literature Review

2.1 Metallurgical characteristics and hardening process

Aluminum alloys are divided into two large groups, wrought alloys and casting alloys. For wrought aluminum alloys, the final products are formed by hot and cold deformations of the continuously or semi-continuously cast half-products. The typical and most known procedures are hot and cold rolling, forging, drawing and extrusion. For casting aluminum alloys, the final product is formed directly without any deformation. The combination of light weight and high strength makes aluminum the ideal component for aircraft industry.

Alloy 2024 T3 belongs in the 2XXX series, of wrought aluminum alloys due to its high strength to density ration and fair corrosion resistance (Figure 2.1). It is widely used for numerous aircraft applications and parts, so it is usually referred to as aircraft alloy. The primary element for this series group is copper, which produces the high strength at the expense of reduced corrosion resistance. These alloys were among the first aluminum alloys developed and were originally called duralumin. Nowadays, 2024 T3 is the most commonly used one in the aircraft industry.

Table 2.1: Wrought Alloy Designation System and Characteristics.

Series Number	Primary Alloying Element	Relative Corrosion Resistance	Relative Strength	Heat Treatment
1xxx	None	Excellent	Fair	Non-heat-treatable
2xxx	Copper	Fair	Excellent	Heat treatable
3xxx	Manganese	Good	Fair	Non-heat-treatable
4xxx	Silicon	Fair	Fair	Non-heat-treatable
5xxx	Magnesium	Good	Good	Non-heat-treatable
6xxx	Magnesium and silicon	Good	Good	Heat-treatable
7xxx	Zinc	Fair	Excellent	Heat-treatable

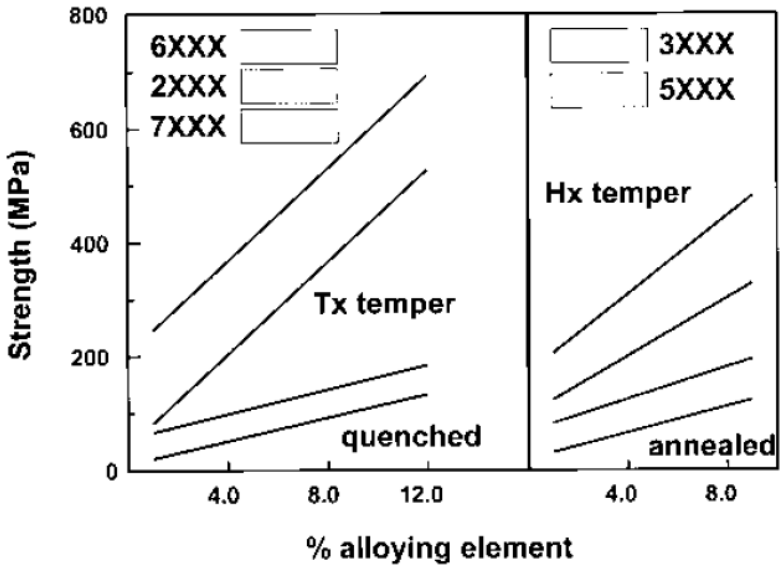

Figure 2.1: Effect of composition and temper on strength of commercial aluminum alloys.[16]

Some alloys (such as 2024) are covered and protected by a thin coating layer of pure aluminum or corrosion-resistant aluminum, so the resulting product is called al-clad. This cladding is metallurgically attached to one or both sides of the sheet or plate and may be 1.5-10% of its total thickness. The base alloy is selected so that it is anodic to the core alloy and protects it from corrosion. Any corrosion that occurs only proceeds to the liner-core interface and then extends laterally, making the cladding very effective in protective especially thin materials.

Heat treatable aluminum alloys like 2024 own their remarkable mechanical properties to age hardening. The thermal treatment for aging of these alloys is a three-stage process:

(1) Solution heat treatment at a relatively high temperature within the single-phase region in order to dissolve the constituents and intermetallics.
(2) Rapid cooling or quenching, usually to room temperature, to obtain a supersaturated solid solution (SSSS) of these elements in aluminum and excess vacancies.
(3) Controlled decomposition of the SSSS to form a finely dispersed precipitate, usually by ageing for specified times at room temperature (natural aging) or at an elevating one (artificial aging) and for one or sometimes two intermediate temperatures.

Table 2.2: Temper Designations for Heat- Treatable Aluminum Alloys[16]

O	Annealed.
F	As fabricated.
W	Solution heat treatment: spontaneous natural aging after solution treatment
T1	Cooled after high-temperature processing and naturally aged to substantially stable condition.
T2	Cooled after high-temperature processing, cold worked and naturally aged to substantially stable condition.
T3	Solution heat-treated, cold worked and naturally aged to substantially stable condition.
T4	Solution heat treated and naturally aged to a substantially stable condition.
T5	Cooled after high-temperature processing and artificially aged.
T6	Solution heat-treated and artificially aged, usually to the maximum strength.
T7	Solution heat-treated and stabilized or overaged.
T8	Solution heat-treated, cold worked and artificially aged.
T9	Solution heat-treated, artificially aged and cold worked.
T10	Cooled after high-temperature processing, cold worked and artificially aged.

For a better understanding of precipitation hardening it is necessary to create a solid solution in which we can achieve a maximum of alloying elements in it. The minimum temperature for solution is only determined by the composition of the alloy, for example the solvus position and the eutectic temperature. So, exceeding the eutectic temperature can lead to incipient melting of eutectic phases which are detrimental for mechanical properties. On the other hand, a low solution temperature can also have a significant effect and desorption on final properties of the alloy.

The second step of the process is quenching which is the critical step during a precipitation treatment. During this step, the SSSS, as well as the vacancies, need to be maintained or even obtained. It is known that the higher the quench rate, the better combinations of strength and toughness can be achieved. The same is true for stress corrosion and corrosion resistance. Furthermore, it is also noticeable that precipitating on grain boundaries and the migration of vacancies to interfaces and grain boundaries do not contribute to the whole aging procedure.

The final step in the precipitation of SSSS requires a fine dispersion of precipitates during aging. It is essential that the aging temperature is below the equilibrium solvus line, as well as, below the GPB solvus line too. Excess vacancies promote diffusion and the formation of zone is substantially faster than the one under equilibrium conditions. During the process, first clusters of solute atoms are formed, followed by the formation of metastable precipitates

The complete decomposition of the SSSS is a complex process, which may involve several stages. Typically, Guinier–Preston–Bagaryatsky (GPB) zones and/or an intermediate precipitate may form prior to the equilibrium phase and may also coexist with the equilibrium phase. The GPB zones are ordered, solute-rich clusters of atoms, which are usually only one or two atom planes in thickness. They retain the structure of the matrix and are coherent with it, although they produce appreciable elastic strains. Their formation requires movements of atoms over relatively short distances, so that they are very finely dispersed in the matrix with densities, which can be as high as 1017 to 1018 cm^{-3}. The intermediate precipitate is normally much larger in size than a GPB zone and is only partly coherent with the lattice planes of the matrix. It has a definite composition and crystal structure which may differ only slightly from those of the equilibrium precipitate. In some alloys, the intermediate precipitate will be nucleated from, or at, the sites of stable GPB zones. In others, this phase nucleates heterogeneously at lattice defects such as dislocations. Formation of the final equilibrium precipitate involves complete loss of coherency with the parent lattice. It forms only at relatively high ageing temperatures and, because it is coarsely dispersed, little hardening results.

Maximum hardening in commercial alloys occurs with the formation of a critical dispersion of GPB zones, an intermediate precipitate, or both. In some cases, the alloys are cold worked (e.g. by stretching 5%) after quenching and before ageing, thus increasing dislocation density and providing more sites at which heterogeneous nucleation of intermediate precipitates may occur. If precipitate particles are widely spaced and large enough, they can be readily bypassed by moving dislocations which bow out between them by a mechanism first proposed by Orowan leaving dislocation rings, as it is almost impossible for a dislocation to overcome the phase boundary between the host lattice and the incoherent precipitation one. The yield strength of the alloy is low, but the rate of work-hardening is high, and plastic deformation tends to spread more uniformly throughout the grains. Accompanying the formation of the intermediate precipitate is the development of few wider, precipitate-free zones adjacent to grain boundaries. These zones are relatively weak with respect to the age-hardened matrix and may deform preferentially leading to high stress concentrations at triple points which, in turn, may cause premature cracking.

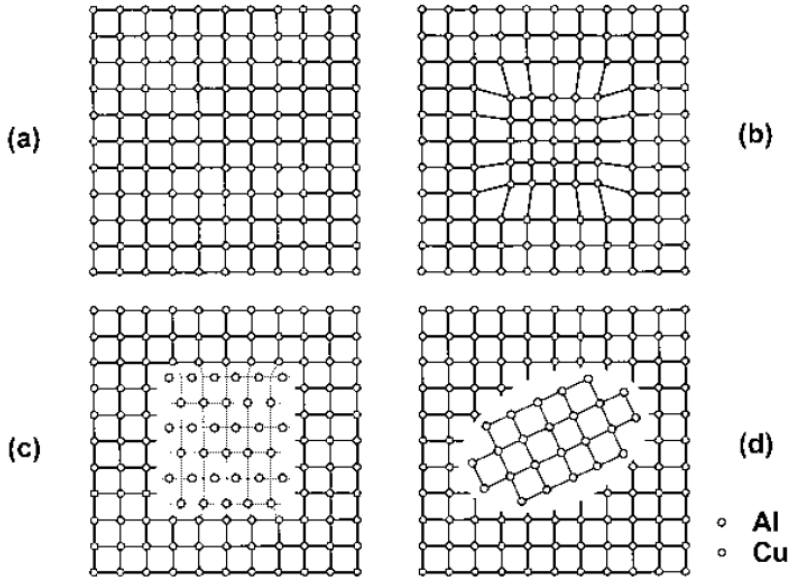

Figure 2.2: Schematic of the different stages during precipitation of aluminum alloys. (a) Solid solution (b) coherent GP zone (c) semi coherent precipitate (d) incoherent equilibrium precipitate.[16]

Table 2.3: The precipitation sequence of 2xxx and 6xxx series alloys[14]

Alloy	Precipitates	Remarks
Al-Cu	GP zones as thin plates on {100} θ" (formerly GP zones)	Probably single layers of copper atoms on {100}$_\alpha$ Coherent, probably two layers of copper atoms separated by three layers of aluminium atoms. May be nucleated at GP zones
	θ' tetragonal Al_2Cu a = 0.404 nm c = 0.580 nm	Semi-coherent plates nucleated at dislocations Form on {100}$_\alpha$
	θ body centred tetragonal Al_2Cu a = 0.607 nm c = 0.487 nm	Incoherent equilibrium phase May nucleate at surface of θ'
AI-Cu-Mg	GP (Cu, Mg) zones as rods along <100>	GP zones form very rapidly in most compositions aged at elevated temperatures. Sometimes known as GPB zones
	S' orthorhombic Al_2CuMg c = 0.718 run b = 0.925 nm a = 0.404 nm	Semi-coherent and nucleated at dislocations Forms as laths in {210}, along <001>,
	S orthorhombic Al_2CuMg a = 0.400 nm b = 0.923 nm c = 0.714 nm	Incoherent equilibrium phase probably transforms from S'. Note that precipitates from the AI-Cu system can also form in compositions with high Cu:Mg ratios
Al-Mg	Spherical GP zones	GP zones solvus below room temperature if <5%Mg and close to room temperature in compositions between 5 and 10%Mg
	β' hexagonal a = 1.002 nm c = 1.636 nm	Probably semi-coherent Nucleated on dislocations - $(0001)_\beta // (001)_\alpha; [01;10]_\beta // [110]_\alpha$
	face centred cubic Mg_5Al_8 (formerly Mg_2Al_3) a = 2.824 nm	Incoherent, equilibrium phase. Forms as plates or laths in grain boundaries and at a surface of β' particles in matrix $(111)_\beta // (001)_\alpha; [110]_\beta // [010]_\alpha$
AI-Mg-Si	Clusters of Mg and Si atoms. GP zones?	GP zones solvus occurs at temperatures that are normally higher than the ageing temperatures
	B'' monoclinic a = 1.534 nm b = 0.405 nm c = 0.683 run p = 106'	Coherent needles, lie along ⟨100⟩a (010) β"// (001) β'†//(001)α;[001]β''//[310]α
	B' hexagonal Mg_2Si a = 0.705 = c = 0.405 nm	Semi-coherent rods, lie along ⟨100⟩a - (0001)β'// (100)α; (10;10)β'//[510]α May form from β''
	B' hexagonal a = 1.04 nm c = 0.405 nm	Semi-coherent laths, lie along ⟨100⟩a - (0001)B'// (001) α; (10;10) B'// [510] α. Forms together with β'; favoured by high Si:Mg ratios.
	B face-centred cubic Mg_2Si a = 0.639 nm	Platelets on {100} May transform directly from, (100) β//(100)α; [110]β//[100]α.

2.2 The corrosion of high strength aluminum alloys

After numerous studies and experimental processes, taking into account the cost and impact of the corrosion phenomenon, it has now become clear that a thorough understanding and effective control of all these corrosion phenomena is essential for reliable extension of aircraft service life and of metallic structures in general.

Aluminum, as indicated by its position in the electromotive force series, is a thermodynamically reactive metal; among structural metals, only beryllium and magnesium are more reactive. Aluminum owes its excellent corrosion resistance to the protective oxide film that is bonded strongly to its surface and that, if damaged, reforms immediately in most environments. The conditions for thermodynamic stability of the oxide film are expressed by the Pourbaix (electrochemical potential versus pH) diagram. Aluminum is passive (protected by its oxide film) in the pH range of about 4 to 8.5. The limits of this range, however, vary somewhat with temperature, with the specific form of oxide film present, and with the presence of substances that can form soluble complexes or insoluble salts with aluminum. Beyond the limits of its passive range, aluminum corrodes in aqueous solutions because its oxides are soluble in many acids and bases, yielding Al^{3+} ions in the former and $A1O^{-}_{2}$ (aluminate) ions in the latter[17].

Corrosion of aluminum in the passive range is localized, usually manifested by random formation of pits. If appreciable attack is confined to a relatively small fixed area of metal acting as an anode, the pits are described as deep. Otherwise, if the area of attack is relatively larger but not so deep, the pits are called shallow.

For aluminum, pitting corrosion is usually caused by halide ions, of which chloride (Cl^{-}) is the most frequently encountered in service. Pitting of aluminum in halide solutions open to the air occurs because, in the presence of oxygen, the metal is readily polarized to its pitting potential. In the absence of dissolved oxygen or other cathodic reactant, aluminum will not corrode by pitting because it is not polarized to its pitting potential. In general, aluminum does not develop pitting in aerated solutions of most non-halide salts for the reason that its pitting potential in these solutions is considerably more noble (cathodic) than in halide solutions, and it is not polarized to these potentials in normal service.

Due to the electrochemical nature of corrosion processes, the relationships between the solution potentials of different aluminium alloys, as well as between potentials of aluminium alloys and those of other metals, are of great importance. Furthermore, the solution-potential relationships between the microstructural constituents of an alloy, significantly influence its corrosion behavior. Compositions of solid solutions and additional phases, as well as the amounts and spatial distributions of the additional phases, can affect both the type and extent of corrosion.

2.2.1 Wrought alloys of 2xxx series

The alloys in the 2xxx series, in which copper is the principal alloying element and often with magnesium as a secondary addition, are less corrosion-resistant than alloys of other series that contain lower amounts of copper. Electrochemical corrosion effects may be stronger in these alloys than in many other types, due to two factors: greater variation in electrode potential with changes in the amount of copper in solid solution; and, under certain conditions, the presence of nonuniformities in the concentration of solid solution. However, the fact that the overall corrosion resistance decreases with increasing copper content is not primarily due to these solid-solution or second-phase solution-potential relationships, but rather to galvanic cells created by the formation of thin copper particles or films deposited on the surface of the alloy as a result of corrosion[17]. As corrosion progresses, copper ions, which initially enter solution, are refilled into the alloy to form metallic copper cathodes. The decrease

in copper ions and the increased effectiveness of O_2 and H^+ reduction reactions in the presence of copper, increase the rate of corrosion

It is generally accepted that pitting constitutes the precursor to any other type of corrosion; pits formation is essentially the first stage of corrosion. Pits first appear in areas where surface abnormalities with respect to the matrix are present. For example, at the grain boundaries, where during the precipitation of second phase intermetallic particles, a neighboring area poor in compound elements is created. If the boundary precipitates are anodic relative to the matrix and the precipitate free zone, then these particles selectively dissolve. Otherwise the neighboring area, which is poor in compound elements, is attacked [18]. In grain boundaries of an alloy belonging to the 2xxx series, for example, they selectively create anodic regions that render the material susceptible to corrosion.

Other researchers have shown that the anodic nature of grain boundaries can be attributed to the segregation in these regions, relative to the grain interior. Guillaumin et al. observed on grain boundaries of 2024 acicular precipitates Al_2CuMg as well as particles of S phase [19]. Generally galvanic cells are formed between regions rich in Cu (S phase) and adjacent areas poor in compound elements. Studies in different corrosive environments have concluded that Cl^- ion is the most aggressive [20]. As a result of the severe presence of Cl^- ions, the marine environment is highly corrosive [21].

2.2.2 Intergranular Corrosion

Another form of corrosion is intergranular (intercrystallite) corrosion, which is a selective attack on the grain boundaries or adjacent areas without appreciable attack of the grain itself. Intergranular corrosion is a general term that includes several variants associated with different metal structures and thermomechanical processes. Intergranular corrosion is caused by potential differences between the grain-boundary region and the adjacent grain bodies. The location of the anodic path varies depending on the different alloy systems, for example in 2xxx series alloys, it is a narrow strip on each side of the copper-depleted boundary. Because intergranular corrosion is involved in SCC of aluminum alloys, it is often presumed to be more deleterious than pitting or general corrosion. However, in alloys which are not susceptible to SCC, intergranular corrosion is usually no more severe than pitting corrosion and tends to decrease over time. For equal depth of corrosion, its impact on resistance effect on strength is also no greater than that of pitting corrosion, although fatigue cracks are more likely to start in areas of intergranular corrosion than at random pits.

2.2.3 Stress corrosion cracking and Corrosion fatigue

Stress-corrosion cracking (SCC) is a term used to describe service failures in engineering materials resulting from the slow environmentally induced crack propagation. The observed crack propagation is the result of the combined and synergistic interaction of mechanical stress and corrosion reactions. This is a simple definition of a complex topic, and like most simplifications, does not define the boundaries of the subject. Environments that cause SCC are usually aqueous and can be condensed layers of moisture or bulk solutions. Typically, SCC of an alloy is the result of the presence of some chemical species in the environment. Thus, chloride ions cause cracking in stainless steels and aluminum alloys [22, 23].

Only aluminum alloys that contain significant amounts of soluble alloy elements, mainly copper, silicon, magnesium, and zinc, are susceptible to SCC. For most commercial alloys, tempers have been developed that provide a high degree of immunity to SCC in most environments.

Stress-corrosion cracking in aluminum alloys is typically intergranular. According to the electrochemical theory, this requires a condition along the grain boundaries that makes them anodic to

the rest of the microstructure so that corrosion selectively propagates along them. Such a state is produced by local solid solution decomposition, with a high degree of continuity of decomposition products along the grain boundaries. The most anodic regions may be either the boundaries themselves (more commonly, the precipitate formed in them) or areas bordering the boundaries that are depleted of the solute.

In 2xxx alloys, the areas with reduced solubility are the most anodic, while grain-boundary regions in other alloys have not been identified with certainty. Strong evidence for the presence of anodic regions and for the electrochemical nature of their corrosion in aqueous solutions is provided by the fact that SCC can be greatly slowed, if not eliminated, by cathodic protection. For alloys requiring microstructural control to avoid susceptibility, resistance is achieved by the use of precipitate-forming processes throughout the microstructure, since the precipitate always forms along boundaries, and its formation usually cannot be prevented [24-28].According to electrochemical theory, susceptibility to intergranular corrosion is a prerequisite for susceptibility to SCC, and the treatment of aluminum alloys to improve resistance to SCC also improves their resistance to intergranular corrosion. For most alloys, however, optimum levels of resistance to these two types of damage require different treatments and thus, resistance to intergranular corrosion is not a reliable indicator of resistance to SCC.

Corrosion fatigue occurs in metals as a result of the combined action of a cyclic stress and a corrosive environment. The corrosion fatigue dependents on the interactions between loads, environmental and metallurgical factors. For a given material, the fatigue resistance (or fatigue life at a given maximum stress value) is generally reduced in the presence of an aggressive environment. The effect varies widely, depending mainly on the metal-environment combination. The environment may affect the likelihood of fatigue cracks initiation, the rate of fatigue crack growth, or even both.

2.2.4Exfoliation corrosion

In certain tempers, the products of wrought aluminum alloys are subjected to exfoliation corrosion, which is sometimes described as lamellar, layer, or stratified corrosion. In this type of corrosion, the attack proceeds along selective subsurface paths parallel to the surface. The layers of uncorroded metal between the selective paths are separated and pressed above the original surface by the voluminous corrosion product formed along the attack paths. Because it can be easily detected at an early stage and is restricted in depth, exfoliation does not cause unexpected structural failure, as does SCC.

Exfoliation occurs predominantly in products with markedly directional structures, where particularly elongated grains form platelets that are thin, relative to their length and width. Susceptibility to this type of corrosion may be due to the presence of aligned intergranular or subgrain boundary precipitates or from aligned strata that differ slightly in composition. The exfoliation intensity is increased in slightly acidic environments or when aluminum is coupled to a cathodic dissimilar metal. Exfoliation is not accelerated by stress and does not lead to SCC. Alloys most susceptible to exfoliation are the heat-treatable 2xxx and 7xxx alloys and certain cold-worked 5xxx alloys. Exfoliation is mainly caused by unfavorable distribution of precipitate. Treatment to eliminate this form of attack promotes either a more uniform granular precipitation or a more advanced stage of precipitation. Thus, increases in the heat treatment time or temperature are equally effective in reducing susceptibility to exfoliation as they reduce susceptibility to SCC.

The occurrence of exfoliation in susceptible materials is significantly affected by environmental conditions. For example, aluminum-copper forged truck pulleys (2024-T4) have been providing

corrosion-free service for many years in the warm climates of the southern and western United States, but exfoliate severely in only one or two years in the northern states, where defrosting salts are used on the highways during the winter months. Exfoliation corrosion initiates between bimetallic couples and progresses along grain boundaries as an intergranular crack. This intergranular crack widens to one crack plane level and widens into multiple crack planes. Corrosive oxides press outward against the adjacent metal, thereby producing a pattern of delamination [29, 30].

2.2.5 Accelerated corrosion tests

Accelerated laboratory tests do not accurately predict long-term corrosion behavior. However, they are often used when we need quick answers to develop new materials. For this reason, accelerated tests are used to detect candidate alloys prior to conducting atmospheric exposures or other field tests. Sometimes, they are also used for quality control tests. Several new laboratory tests for exfoliation corrosion have been standardized in recent years under the jurisdiction of American Society for Testing and Materials (ASTM) Committee G- 1 for corrosion of metals.

ASTM G 34 provides an accelerated exfoliation corrosion test for 2xxx and 7xxx alloys by continuous immersion of test materials in an aqueous solution containing 4 M NaCI, 0.5 M potassium nitrate (KNO_3), and 0. 1 M HNO_3 at 25 ºC. Susceptibility to exfoliation is determined by visual examination, using performance ratings established by reference standard photographs [31]. This method, known as the EXCO test, is primarily used in research, development and quality control of such mill products as sheet and plates. However, it should not be considered as the optimum quality acceptance method. Rather, this method provides a useful prediction of the exfoliation behavior of these alloys in various types of outdoor services, especially in marine and industrial environments. The test solution is very corrosive and is intendent (maybe *'intended'*?) to represent the more severe type of environmental exposure.

It remains to be determined whether correlations between EXCO test ratings and practical service conditions for a given alloy can be determined. Outdoor exposure tests shall be carried out for this purpose. For example, it has been reported that samples of 7xxx alloys rated EA (superficial exfoliation) or P (pitting) in 48 h EXCO test did not develop more than superficial exfoliation (EA rating) over a six to nine-year exposure to seacoast atmospheres, whereas materials rated as EC or E (severe and very severe exfoliation, respectively) developed severe exfoliation within one to seven years at the seacoast. An additional comparison is expected as outdoor testing is extended.

2.3 Hydrogen Damage in Alloys

2.3.1 General Classification of Hydrogen Damage

Hydrogen damage is a form of environmentally assisted failure that is happening most of the times from the combination of hydrogen penetration and applied or residual tensile stress. To some specific alloys or groups of alloys, hydrogen damage manifests itself in many ways, such as blistering, cracking, hydride formation and loss in tensile ductility. During the past decades, these kinds of failures have been collectively termed as hydrogen embrittlement, although they have been erroneously mistaken for other forms of environmentally induced failures. This term, while not properly describing the phenomenon, continues to be used although a multitude of failure modes involving hydrogen do not demonstrate the classical features of embrittlement, which is reduced load carrying capability and/or fracture below the yield strength. In order to enhance the understanding of the factors that cause this behavior in alloys and to provide a basis for the development and analysis of theories regarding different hydrogen damage

mechanisms, a categorization of specific types of hydrogen damage has been organized. More specifically:

Blistering forms predominantly as a result of atomic hydrogen diffusing to internal defects, such as laminations or nonmetallic inclusions. Being incredibly reactive, hydrogen atoms combine with each other conducting the creation of hydrogen gas (H2). The produced pressure of molecular hydrogen can attain such high values that localized plastic deformation of the alloy occurs, there is a degradation of mechanical properties leading to failures such as rupture even under light loading stress. Shatter cracks, flakes, and fisheyes are typical examples to hydrogen damage in forgings, castings, and weldments. These failures are attributed to hydrogen pickup during the manufacturing process.[51].

Hydrogen environment embrittlement occurs when hydrogen bearing gases encounter the alloys during plastic deformation, or if there is an exposure to a corrosion reaction. This drives to a dependent strain rate which in many cases leads to degradation of the mechanical properties.

Hydrogen stress cracking often referred to as hydrogen-induced cracking or static fatigue is characterized by the brittle fracture of a normally ductile alloy under sustained load in the presence of hydrogen. Most often, fracture occurs at sustained loads below the yield strength of the material. Hydrogen stress cracking is associated with absorption of hydrogen and a delayed time to failure (incubation time) during which hydrogen diffuses into regions of high triaxial stress. The catastrophic cracking of steels in hydrogen sulfide (H2S) environments referred to as sulfide stress cracking is a special case of hydrogen stress cracking [50].

Hydrogen attack is a form of hydrogen damage attributed to exposure to high pressure hydrogen at high temperatures and for extended time. Hydrogen infiltrates the alloys either as a carbide or in solution and leads to the formation of methane gas. This leads to the formation of fissures, cracks and flakes or simply decarburize the alloys, such as steel which means the main element resulting in strength weakens and so does the strength of the alloy. This form of damage is temperature dependent, with a threshold temperature of approximately 200 ^{o}C [52, 53].

Loss in tensile ductility was one of the earliest recognized and most well-known forms of hydrogen damage. Decrease in the elongation is observed for steels, stainless steels, nickel-base alloys, aluminum alloys, and titanium alloys exposed to hydrogen. Lower-strength alloys are the one which are most affected by this mode of failure. Loss in tensile ductility behavior is very sensitive and directly linked to strain rate, so it becomes more pronounced as the strain rate decreases [54].

Degradation in flow properties in hydrogen environments has been found at ambient temperatures for iron and steel and at elevated temperature for several alloy systems. The steady-state creep rate under constant load has been observed to increase in the presence of hydrogen for some nickel-base alloys. Hydride formation produces embrittlement in magnesium, tantalum, niobium, vanadium, uranium, thorium, zirconium, titanium, and their alloys, as well as many other less common metals and alloys. The degradation of mechanical properties and the cracking of these metals and their alloys are attributable to the precipitation of metal hydride phases. Hydrogen pickup often results from welding, heat treating, charging from a corrosion process, or during melting of the alloy.

Hydride formation is enhanced for some metal-hydrogen systems by the application of the so-called stress-induced hydride formation. Most of the alloys that form hydrides are generally ductile at both high and low temperatures, for example over 300 ^{o}C for the former and less than 100^{o}C for the latter. This behavior attributed to the temperatures is identical to the one observed for the hydrogen embrittlement of nickel and ferrous alloys. The main failure that's observed is ductile rupture.

2.3.2 Mechanisms of Hydrogen Embrittlement

As can be estimated from the numerous categories of hydrogen damage, there are many theories for these various forms of degradation. The main theories for hydrogen damage are based on pressure, decoupling, hydrogen attack, surface adsorption, plastic flow and hydrite formation. Although many other explanations have come forward, most of them are variations on these basic models.

The *pressure theory* of hydrogen embrittlement is one of the oldest models for hydrogen damage. This theory attributes hydrogen embrittlement to the diffusion of atomic hydrogen into the metal and its eventual accumulation at voids or other internal surfaces in the alloy. As the concentration of hydrogen increases at these microstructural discontinuities, a high internal pressure is created that enhances void growth or initiates cracking. As mentioned before, this mechanism is responsible for blistering and loss in tensile ductility, nonetheless it does not explain main of the factors that have been observed for different types of failures. However it is considered to be a well-recognized phenomenon which either with the use of high pressure hydrogen gas or under electrochemical charging, diffuses the hydrogen into the alloy and can create a significant density of voids and irreversible damage to the alloy consistent with a pressure-dependent model [32].

The *surface adsorption theory* indicates the hydrogen adsorbs on the free surfaces as a result of tip cracking, leading to the degradation of surface free energy and thus the work of fracture. This means that crack propagation would be enhanced at lower stress level that are typically experienced for alloys exposed in benign environment. One argument put forward by those you are against this theory is that it greatly underestimates the work of fracture and does not account for the discontinuous crack growth that has been observed for hydrogen cracking.

Decohesion relates the cohesive force between atoms of the alloy matrix with the effect of hydrogen absorption. The maximum cohesive force between metal atoms is lowered when high hydrogen concentrations are achieved ahead of a crack tip, for example the local maximum tensile stress perpendicular to the plane of the crack then becomes equivalent to or greater than the lattice cohesive force and fracture results.

Enhanced plastic flow is associated with hydrogen-dislocation interactions and is primarily based on fractographic observations. This approach proposes that atomic hydrogen enhances dislocation motion, generally screw dislocations, and the creation of dislocations at surfaces and/or crack tips leading to softening of the material on a localized scale [33, 34]. This behavior has only been confirmed in certain type of steel in addition to the fact that hydrogen can cause a severe hardening to the alloy. High resolution means of light and electron microscopy have revealed enough evidence of crack tip plasticity as well as intergranular fracture surface and brittle cleavage in support of this mechanism and theory

Hydride formation is the degradation of Group Vb metals (niobium vanadium. and tantalum) and zirconium, titanium [35] and magnesium in hydrogen environments by the formation of a brittle metal hydride at the crack tip. The presence of large quantities of hydrogen diffused in the alloy, leads to the precipitation of a metal hydrate. By cracking, this hydrate creates a chain reaction of crack arrests in the more ductile matrix, mainly ahead of the crack top, leading to a continued crack growth between the formed hydrates throughout the alloys. This failure mechanism is called ductile rupture and the application of stress increases its effect. The precipitation of new hydrites is repeated and so does the cleavage of these hydrides until fracture is complete.

Hydrogen Trapping. Many different theories and models have been attributed to hydrogen damage, but the behavior and the impact of hydrogen into the alloy has not been yet clarified. One of the principal factors that determine the hydrogen damage susceptibility of various alloys is a phenomenon referred to as trapping. Experiments and diffusion studies in other type of alloys like steels and iron have shown an initial delay in the diffusion rate towards the interior of the alloy, followed by a steady-state diffusivity compatible with that expected theoretically is achieved .This retardation is directly related to the filling of traps by hydrogen Another noticeable observation is that diffusivity of hydrogen, mainly in steels, corelates with the increasement in concentration of particles (traps), more precisely showing a decreased rate. Hydrogen trapping can be considered as the binding of hydrogen atoms to impurities, structural defects, or microstructural constituents in the alloy. Binding may be attributed to local electric fields and stress fields, temperature gradients, chemical potential gradients, or physical trapping. These hydrogen traps may be mobile (dislocations. stacking faults) or stationary (grain boundaries, carbide particles, individual solute atoms)[38, 39]. They may also be reversible or irreversible traps. Short duration trapping of hydrogen in which the occupancy time is limited is referred to as reversible. A long residency time for hydrogen characterized by a high binding energy is termed irreversible trapping [40, 41].

2.3.3 Hydrogen Damage in Al Aloys

Only during the last few decades, it has been determined that hydrogen embrittles aluminum. Industrial processes yielding aluminum products are normally conducted in environments containing hydrogen sources from which they absorb gas as a contaminant. These products are vulnerable to hydrogen absorption because the solubility of the gas in the solid metal is low. The damage is due to internal or sub-surface defects that are essentially extensive hydrogen traps of one form or another, some inherited from unsoundness and inclusions in castings and ingots, while others introduced during subsequent heat and mechanical processing of the solid metal in course of fabrication to semi-finished products. Typical examples of damage are blistering or other surface blemishes on heat-treated laminated sheets and extrusions, discontinuities in load-bearing sections, inadequate surface finish for anodic quality products and inability to retain fluids in near-net shape castings.

More specifically, testing in specific hydrogen environments has revealed the susceptibility of aluminum to hydrogen damage. Hydrogen damage in aluminum alloys may take the form of intergranular [42] or trans granular cracking or blistering. Blistering is most often associated with the melting or heat treatment of aluminum, where reaction with water vapor produces hydrogen. Blistering due to hydrogen is frequently associated with grain-boundary precipitates or the formation of small voids. Blister formation in aluminum is different from that in ferrous alloys in that it is more common to form a multitude of near-surface voids that coalesce to produce a large blister.

In a manner like the mechanism in iron-based alloys, hydrogen diffuses into the aluminum lattice and collects at internal defects. This occurs most frequently during annealing or solution treating in air furnaces prior to age hardening [43].

Dry hydrogen gas is not detrimental to aluminum alloys; however, with the addition of water vapor, subcritical crack growth increases dramatically. The threshold stress intensity for cracking of aluminum also decreases significantly in the presence of humid hydrogen gas at ambient temperature [44].

Crack growth in aluminum in hydrogen is also a function of hydrogen permeability, as in the iron- and nickel-base alloys. Hydrogen permeation and the crack growth rate are a function of potential, increasing with more negative potentials, as expected for hydrogen embrittlement behavior. Similarly, the ductility of aluminum alloys in hydrogen is temperature depended displaying minimum in reduction

in area below 0°C, this is similar to other fcc alloys. Most of the work on hydrogen embrittlement of aluminum has been on the 7xxx alloys; therefore, the full extent of hydrogen damage in aluminum alloys has not been determined and the mechanisms have not been established. Some evidence for a metastable aluminum hydride has been found that would explain the brittle intergranular fracture of alurninum-zinc-magnesium alloys in water vapor. However, the instability of the hydride is such that it has been difficult to evaluate. Another explanation for the intergranular fracture of these alloys is that there is preferential decohesion of grain boundaries containing segregated magnesium. Overaging of these alloys increases their resistance to hydrogen embrittlement in much the same way as for highly tempered martensitic steels. Regarding corrosion-induced material embrittlement, Pantelakis et al. [11, 45] claimed that hydrogen embrittlement could be responsible for the dramatic degradation of toughness and ductility of 2091 and 8090 Al-Li alloys as well as conventional 2024 alloy in several types of accelerated corrosion tests [46]. In other alloy systems there is mounting evidence connecting embrittlement and stress corrosion cracking to hydrogen penetration. Speidel [8] reviews recent results, mainly for Al-Mg-Zn alloys. Studies by Scamans et al. [47] of Al embrittlement in humid air, point to the major role of hydrogen. In particular, the intergranular crack path and the reversibility of the phenomenon (recovery of ductility after degassing) support a hydrogen, rather than an anodic dissolution, mechanism. Also, Scamans and Tuck [48] measured H_2 permeability and stress corrosion resistance of the Al-Mg-Zn alloy, as functions of quench- rate and aging treatment, and found similar trends. However, the stress-corrosion-resistant Al-Mg-Si alloy does not allow hydrogen permeation through its matrix, though the volume of hydrogen produced by surface reaction with the water in humid air is even higher than that of the Al-Nig-Zn alloy [48]. It has been suggested [8] that hydrogen plays a major role in stress corrosion cracking of aluminum alloys exposed to aqueous solutions as well. An indication in favor of this argument is provided by measurement, in Al-Mg-Zn alloys, of hydrogen permeation and stress corrosion crack growth rates [49]. These parameters are found to vary similarly as functions of the electrode potential. Despite the lack of a universally accepted hydrogen embrittlement mechanism, a generally recognized common feature is that some critical concentration of hydrogen must build up at potential crack sites, for failure to initiate. Thus, the distribution of hydrogen inside the metal and its pattern of migration are of paramount importance in understanding the phenomena and designing alloys with improved behavior.

It has been shown [50, 51] that lattice defects (vacancies, dislocations, grain boundaries) and precipitates provide a variety of trapping sites for diffusing hydrogen. Hydrogen traps have mechanistically been classified by Pressouyre [40] as reversible and irreversible, depending on the steepness of the energy barrier needed to be overcome by hydrogen to escape from the trap. For example, during a degassing experiment reversible traps will release hydrogen continuously, while irreversible ones will do so only after a critical temperature has been reached. This is the temperature at which the probability of a single jump out of the steep trap becomes nonnegligible. Reversible and irreversible traps may play different roles during an actual experiment [41]. In particular, irreversible traps will always act as sinks for hydrogen, whereas reversible traps may act as sinks or sources depending on initial hydrogen charging of the lattice. A uniform distribution of irreversible traps is believed to provide a beneficial effect in alloy behavior under embrittling conditions, by arresting diffusing hydrogen and thus delaying its buildup at the crack sites [38, 52]. When crack nucleation and growth is along the grain boundaries, boundary chemistry may be playing an important role. Various studies on Al-Mg-Zn alloys have indicated that alloying elements (and in particular Mg) are segregated on the grain boundary. Tuck [53] proposed that Mg hydride forms at grain boundaries and is responsible for material embrittlement. In an effort to explain the connection between Mg-H interaction and material embrittlement, Song et al. [54] recently showed that stress corrosion and fatigue crack growth rates increase with the concentration of solid solution Mg on grain boundaries. The same authors theoretically calculated a decrease in the

intergranular fracture work with both Mg and H segregation. Other aluminium alloys that have been studied for hydrogen induced failure are 8090 [55, 56] and 7050 [54].

Useful insight in the nature and intensity of hydrogen traps can be offered by studying the temperature needed to break these bonds. Thus, thermal analysis techniques have been used for a variety of alloys [53, 57]. In particular, thermal desorption has been successfully used to study hydrogen partitioning in pure cast aluminum and in Al-Cu and Al-Mg_2Si alloys [51] and hydrogen diffusion in Al-Li alloys. Among other findings, these studies show that, for aluminum alloys, the energy of chemisorption is lower than the energy for lattice diffusion. Thus, the layer of passive oxide-formed on the surface of aluminum alloys-does not mask the bulk trapping states, and the results of thermal analysis are meaningful. Accelerated corrosion tests were recently used by Haidemenopoulos et al. [58] to characterize corrosion and hydrogen absorption in the less studied but widely used Al-Cu alloy 2024. In [59] hydrogen evolution from the corroded specimen of Al alloy 2024 was systematically measured as a function of temperature. The exfoliation test [31] was used as an accelerated corrosion method, and different exposure times were tested. The existence of multiple trapping states was verified, and the quantity and evolution pattern of hydrogen is discussed.

Chapter 3 - Experimental procedure

3.1 Materials Studied

As discussed earlier, the focus of this research was aluminum alloys belonging to the 2xxx alloy series, more accurately, alloy 2024 T3. The material was obtained in plate form, that had not been anodized and its only surface protection emanated from the thin protective oxide, which is created when the material is exposed to atmospheric air. Material was obtained from several suppliers and with thickness 3.2mm.

The chemical composition of the material is displayed in Table 3.1and the thermal treatments of the alloys are presented in Table 3.2 below.

Table 3.1: Chemical composition of alloys of aluminum (%wt.).

Sample	Al	Si	Fe	Cu	Mn	Mg	Cr	Zn	Ti	Other
2024	90,7-94,7%	0,50%	0,50%	4,35%	0,60%	1,5%	0,10%	0,25%	0,15%	0,15%

Table 3.2: Thermal treatments of aluminum alloys.

Material	Temperature Dissolution	Quenching	Cold rolling	Thermal treatment
2024 Bare	495 °C	0°C	No	160°C 150°C 120°C

The labeling scheme used to identify the orientations and planes of the alloys is shown in Figure 3.1.

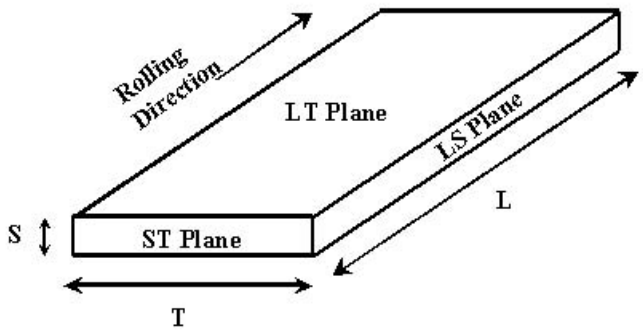

Figure 3.1: Labelling scheme used for directions and planes.

3.2 Microstructural characterization

All specimens were prepared using classical metallographic techniques. The non-corroded specimens were cut from the plate of the corresponding material with the use of a robotic arm microtome (Struers Accutom). Their size was roughly 0,5 x 1cm².The specimens for metallographic observation were placed in simple epoxy resin (Acryfix) that stabilizes in atmospheric temperature (20-25^{0}C) in roughly 10-15 minutes. The specimens were placed in epoxy resin for easy handling.

The resin fills the pores, voids and surface abnormalities of the specimen. This process is essential for the maintenance of pits and microcracks during the next steps of preparation. The surface planes under observation were the rolling surface and the side surface (LT and LS plane in **Error! Reference s ource not found.**. Subsequently the specimens were initially grinded on SiC abrasive wheels. The sizes of grains were 220, 320, 500, 800, 1000, 2000 grid. Polishing of the specimens followed on special disks with diamond paste of 3μm and 1μm grain size respectively. The last stage of preparation was polishing with Al_2O_3 particles of 0,45μm and 0,01μm diameter successively. Finally, the surface was chemically etched with Keller's reagent. This reagent has a chemical composition of *2,5 ml HNO_3, 1,5 ml HCl, 1,0 ml HF and 95,0 ml H_2O*. The time of exposure in Keller's was a few seconds. Finally the specimens were washed with distilled water and alcohol and dried in a purge of warm air [60].

3.3 Accelerated corrosion testing

Accelerated corrosion testing that provides a useful simulation of the exfoliation behavior of these alloys in various types of outdoor service, especially in marine and industrial environments, was employed. The accelerated corrosion test (EXCO) is described in ASTM specification G34-90 [31]. It includes exposure at 22°C for 24h, in a solution containing 234g NaCl, 50g KNO_3 and 6,3ml concentrated HNO_3 (70%wt) diluted to 1 L of distilled water. The quantity of solution used is proportional to the specimen external surface area, with the minimum amount required being 10 ml for every cm^2 of specimen surface and the maximum 30ml. Specimen cleaning, after removal from the corrosive solution involved soaking in concentrated HNO_3 (70%wt) for 5 minutes, rinsing in distilled water, then in acetone and thoroughly drying in a purge of warm air. The entire cleaning process did not exceed 10 minutes and fishing line was used to place the specimens in the center of the pot so all 6 surfaces where corroded equally. Then, half of the specimens were placed in simple epoxy resin for metallographic observation and others were used for the determination of hydrogen quantity trapped in the material's microstructure.

3.4 Heat treatment

Some specimens were surface cleaned with alcohol according to ASTM G1 and then were heat treated. The specimens got all artificially aged, after solid solution at 495^{o}C for 30 min. Different artificial aging conditions were performed for the total 66 specimens at 160 ^{o}C, 150 ^{o}C and 120 ^{o}C, in an electric oven with ±5 ^{o}C temperature control and for different times.

The aging temperatures were selected in order to affirm the results of the artificial aging of the commercial sheet AA2024-T3, according to a paper by Alexopoulos et al. [61]. Aging times were selected to correspond to all aging conditions, including Under-Aging (UA), Peak-Aging (PA) and Over-Aging (OA). The available specimens were exposed for 24h to the laboratory exfoliation corrosion (EXCO solution) according to specification ASTM G34. Then, half of the specimens were placed in simple epoxy resin for metallographic observation and others were used for the determination of hydrogen quantity trapped in the material's microstructure.

3.5 Scanning Electron Microscopy (SEM)

Surface analysis was performed to the corroded specimens provided by the tests performed. Images were acquired with a Jeol Scanning Electron Microscope in the secondary electron mode with an accelerating voltage of 30 KV.

The scope of this work was to investigate the appearance of the corroded surface in order to determine pitting sites and other modes of corrosion. As corroded specimens with different tempers were examined the difference was correlated with corrosion, microstructure and heat treatment.

The outcome of the metallographic analysis was also combined with the hydrogen content measurements and provided evidence of possible hydrogen embrittlement.

After the heat treatment tests, the specimens were placed in the SEM microscope mention above for examination. The study of the surface correlated with the corrosion results and the hydrogen measurements will lead to a spherical understanding of hydrogen embrittlement.

So, immediately after corrosion the specimens were immersed in concentrated nitric acid (70%) for 5 minutes, in order to remove the corrosion products deposited during electrochemical action. Finally, they were dried in a purge of warm air. For the observation in SEM it is essential that the conductivity of specimens during observation is ensured, therefore the specimens were affixed on the special specimen holder with graphite paste. Then they are placed in the vacuum chamber of the microscope for the observation.

3.6 Hydrogen measurements

A main part of this thesis consists of the determination of hydrogen concentration and it's trapping states in the material after corrosion. The determination of these states was conducted by using a thermal desorption technique (TDS).

The scope of this process was to measure the amount of hydrogen eluting from specimens previously subjected to various periods of exfoliation corrosion exposure as a function of temperature. Strips of the materials, 3.2mm wide and 20 mm long, were cut at right angles to the rolling direction and were exposed to exfoliation corrosion. The large surface to volume ratio of the specimen was chosen with a view to decreasing the hydrogen evolution time and increasing the sensitivity of the measurements. The exfoliation accelerated corrosion test is described in ASTM specification G34-90 as is mentioned above. Hydrogen evolved from the corroded specimen with controlled heating in an inert atmosphere and was measured using a gas chromatograph.

For the determination of hydrogen quantity trapped in the material's microstructure an in-house experimental setup was used. This setup consists of a furnace with a system of automatic temperature control, a supply of inert gas (high-purity nitrogen) and a gas chromatograph equipped with a valve for sampling gases. The sample was placed in a 10 mm diameter quartz tube and held in place by an inert porous diaphragm, permeable to the gas (quartz wool). The tube was inserted in the furnace and subjected throughout the experiment to a flow of Q=20ml/min high purity nitrogen. This flow was then driven to a gas chromatograph equated with a TCD detector. Calibration runs were performed using standard H_2 – N_2 mixtures, of volume concentration 1000 and 10000 ppm. Blind experiments were

conducted with an empty tube heated up to 600ºC and no hydrogen was detected. The temperature of furnace was increased at a rate of approximately 5º C/min and the nitrogen current swept along everything that was emitted by the sample and carried it in the gas chromatograph. The sampling was performed manually through the gas-sampling valve about every 2 minutes.

Primary data consist of curves of the intensity, I, of TCD detector signal (in μV) versus time, combined with the temperature history of the specimen. Detector intensity is converted to hydrogen mass flow rate, m, by the expression

$$m=\alpha IQ$$

where α has units of g of H_2/ (ml μV). It is the calibration constant of the detector expressing the mass concentration of hydrogen per μV indication of the detector. During the present work, a small deterioration of the accuracy of the detector was witness, which was considered in the data.

The results reported in the next section are presented as hydrogen mass flow rate (in μg/min) versus specimen temperature. If the heating rate is sufficiently low, each trapping site produces an independent peak. The temperature of the onset of peak growth is characteristic of the energy needed to release hydrogen from the respective trapping site. Thus, low temperature peaks are related to weakly bonded hydrogen and high temperature peaks to strongly bonded hydrogen. Calculation of the total hydrogen quantity in each trapping site is performed by integrating the area under the respective peak.

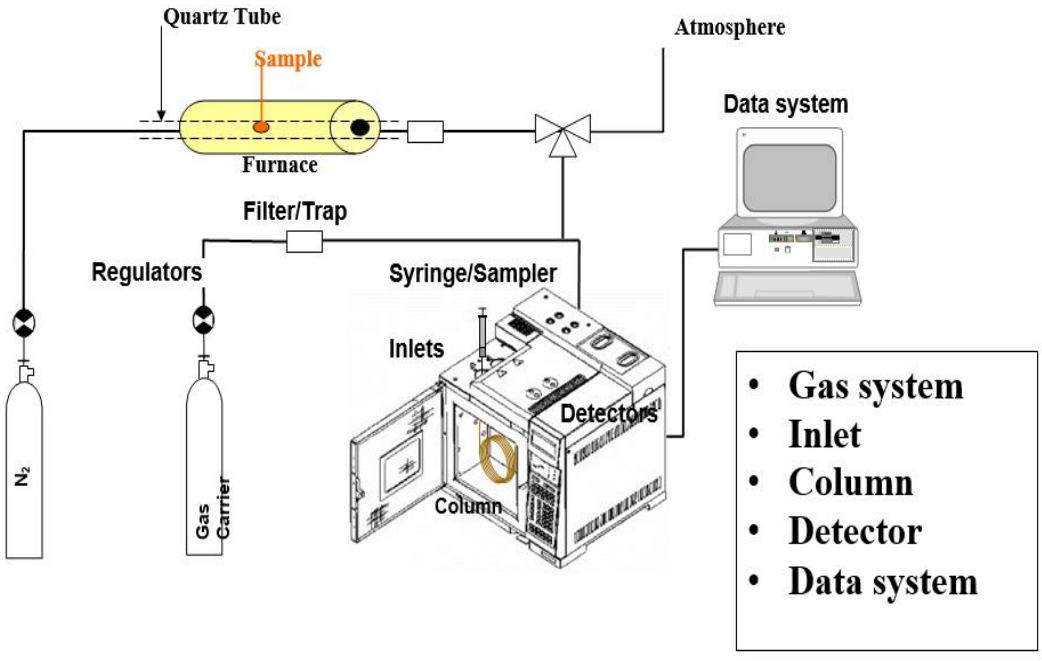

Figure 3.2: Thermal Desorption Spectroscopy setup

Chapter 4 – Results and Discussion

4.1 Metallography-Microstructural Characterizations

Characterization of microstructure after heat treatment and corrosion tests was performed by means of light optical metallography (LOM). Metallography was performed on cross section of the specimens. Specimen preparation for metallography involved cutting with a Struers Minitom machine, grinding with SiC papers whose sizes of grains were 220, 320, 500, 800, 1000, 2000 , 2400 grid and polishing with Struers clothes Struers diamond pastes of 3 and 1 μm respectively. The last stage of preparation was polishing with Al_2O_3 particles of 0,45μm and 0,01μm diameter. Etching was performed by immersing the specimen into Keller's reagent (2.5mL HNO_3, 1.5mL HCl, 1.0mL HF diluted in 95mL H_2O). Optical metallography was performed on an Aristomet inverted microscope at magnifications 200X – 500X. Although the grain bountaries are visible in all cases, we cannot extract any kind of remarkable differences since the scale of μm is very restricting. Below from **Error! Reference source n ot found.** to **Error! Reference source not found.** are depicted the metallographies for different aging times.

Aging time- 1 hours

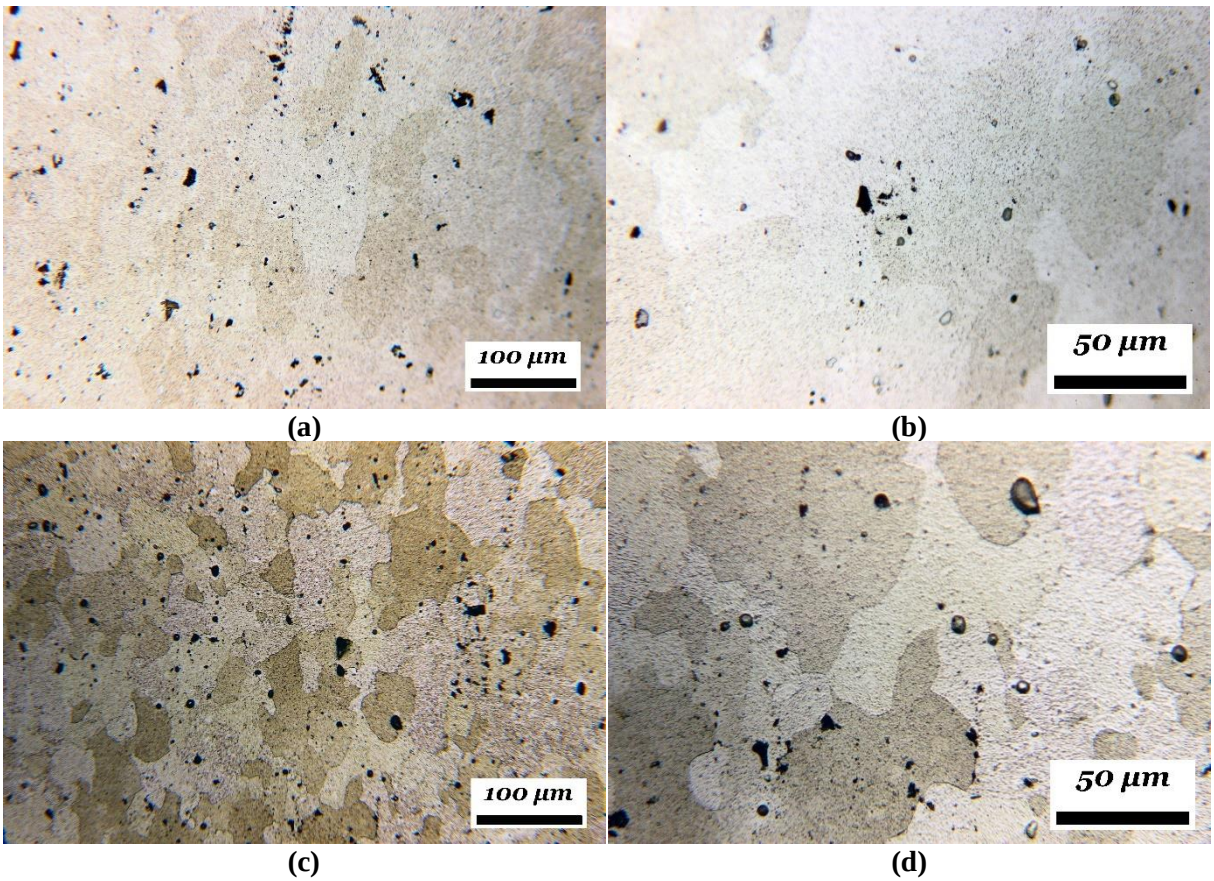

Figure 4.1: Metallographic images from the surface of the specimens (LT plane).Images (a) and (b) depict the fracture after artificial aging at 150°C while (c) and (d) after artificial aging at 160°C. Magnifications used are x200 for (a)&(c) and x500 for (b)&(d). Aging time was 1 hour in all cases.

Aging time- 8 hours

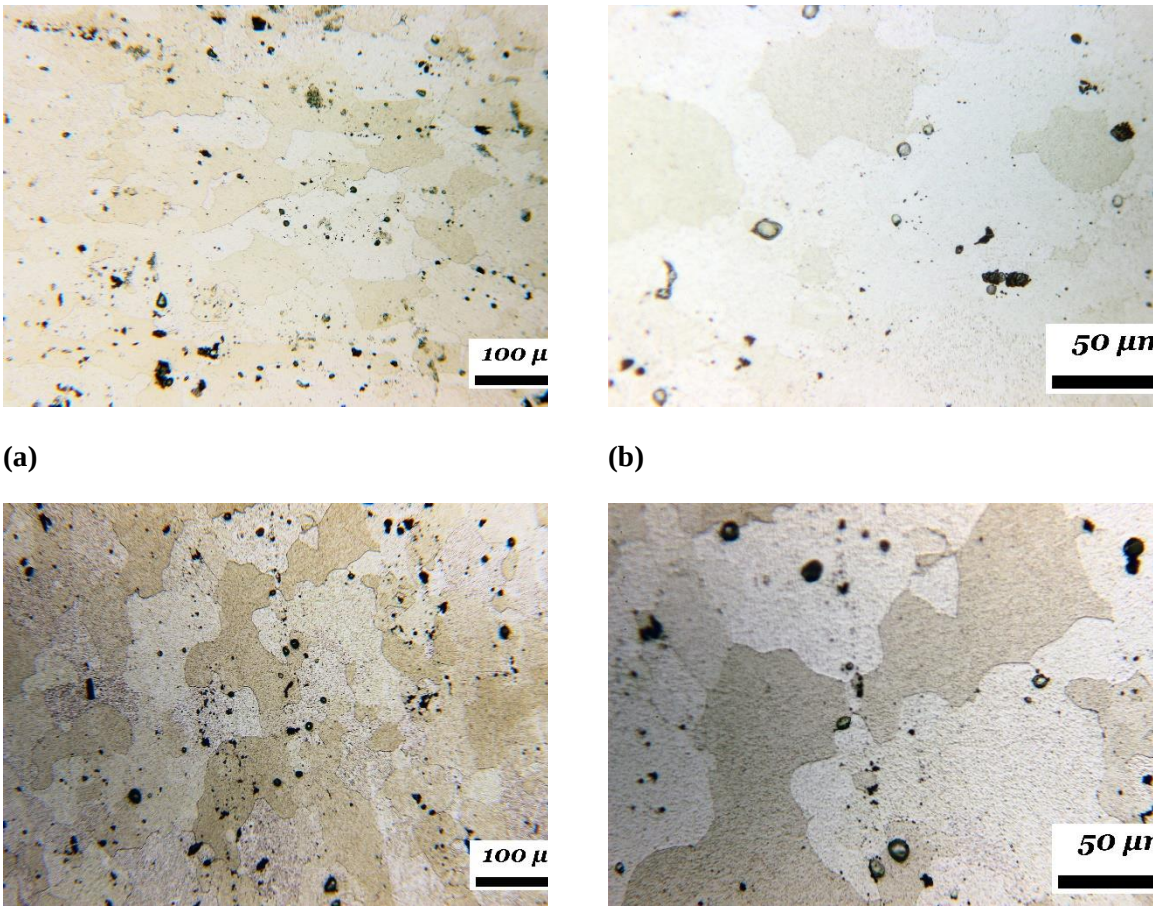

(a) **(b)**

(c) **(d)**

Figure 4.2: Metallographic images from the surface of the specimens (LT plane).Images (a) and (b) depict the fracture after artificial aging at 150ºC while (c) and (d) after artificial aging at 160ºC. Magnifications used are x200 for (a)&(c) and x500 for (b)&(d). Aging time was 8 hours in all cases.

Aging time- 24 hours

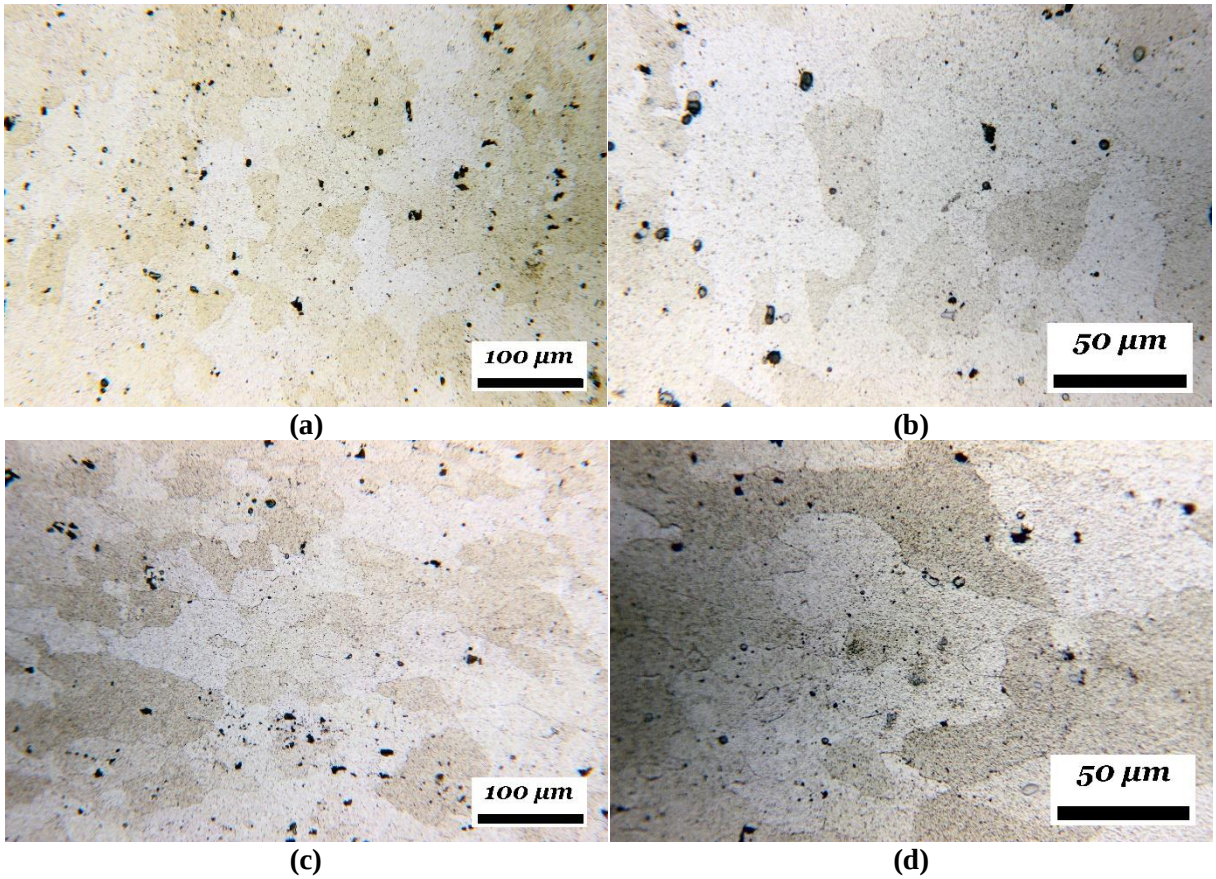

(a) **(b)**

(c) **(d)**

Figure 4.3: Metallographic images from the surface of the specimens (LT plane).Images (a) and (b) depict the fracture after artificial aging at 150ºC while (c) and (d) after artificial aging at 160ºC. Magnifications used are x200 for (a)&(c) and x500 for (b)&(d). Aging time was 24 hours in all cases.

Aging time- 48 hours

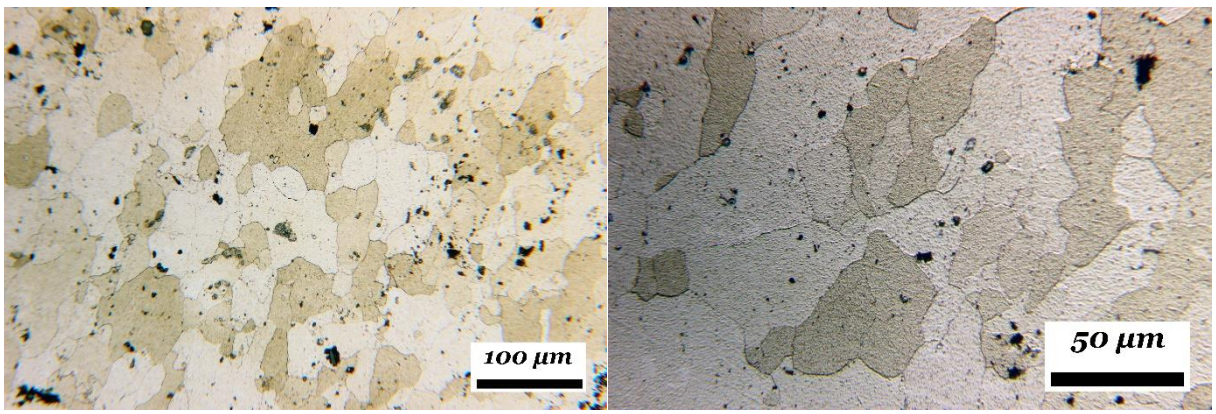

(a) **(b)**

Figure 4.4: Metallographic images from the surface of the specimens (LT plane).Both images depict the fracture after artificial aging at 150ºC. Magnifications used are x200 for (a) and x500 for (b). Aging time was 48 hours in all cases.

Aging time- 72 hours

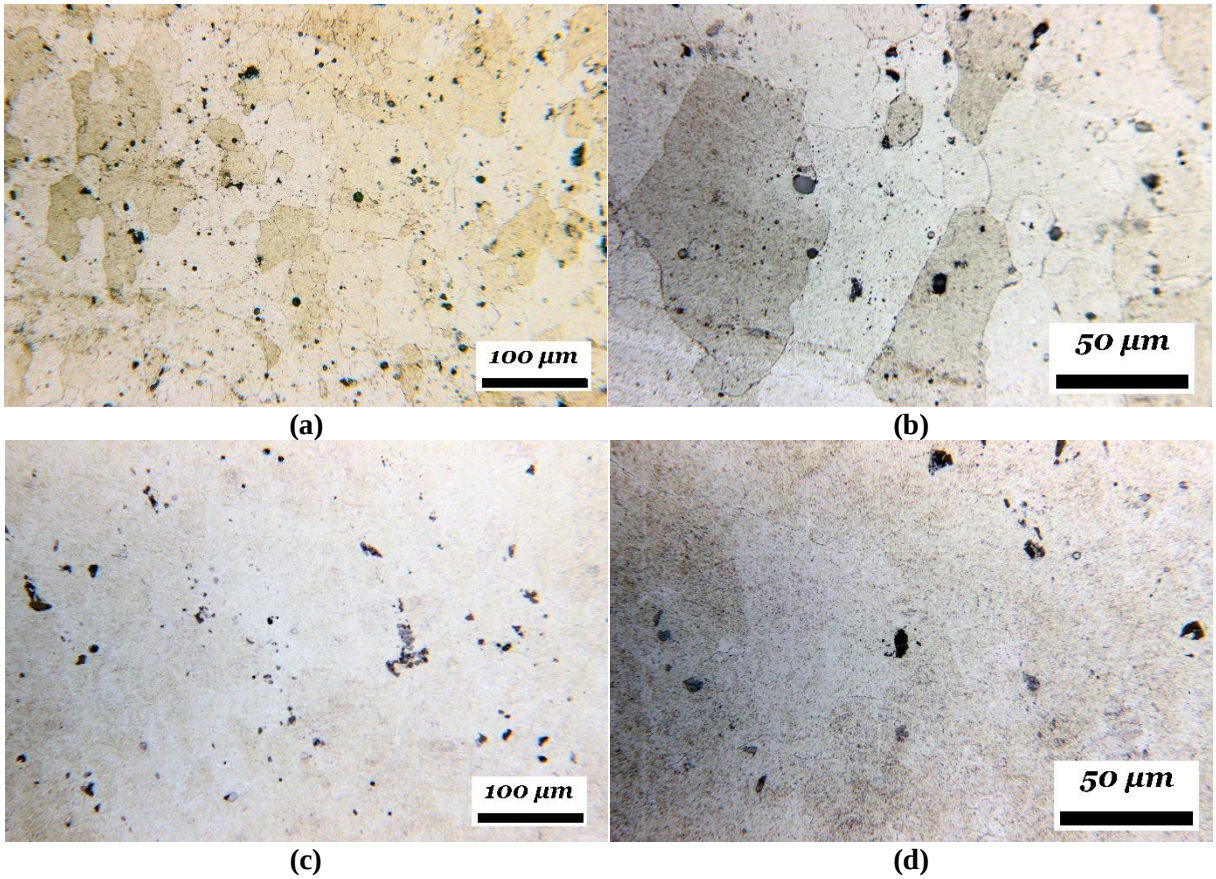

(a) **(b)**

(c) **(d)**

Figure 4.5: Metallographic images from the surface of the specimens (LT plane).Images (a) and (b) depict the fracture after artificial aging at 150ºC while (c) and (d) after artificial aging at 160ºC. Magnifications used are x200 for (a)&(c) and x500 for (b)&(d). Aging time was 72 hours in all cases.

Aging time- 96 hours

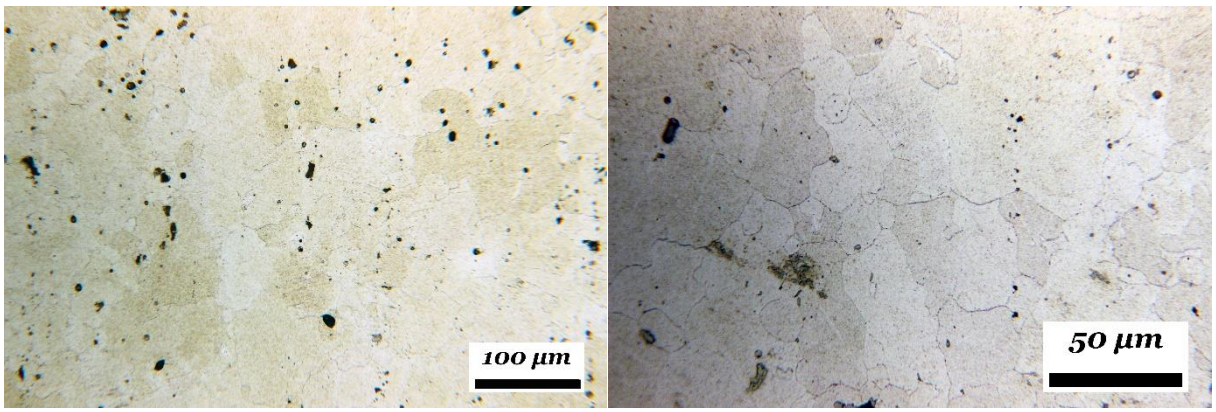

(a) **(b)**

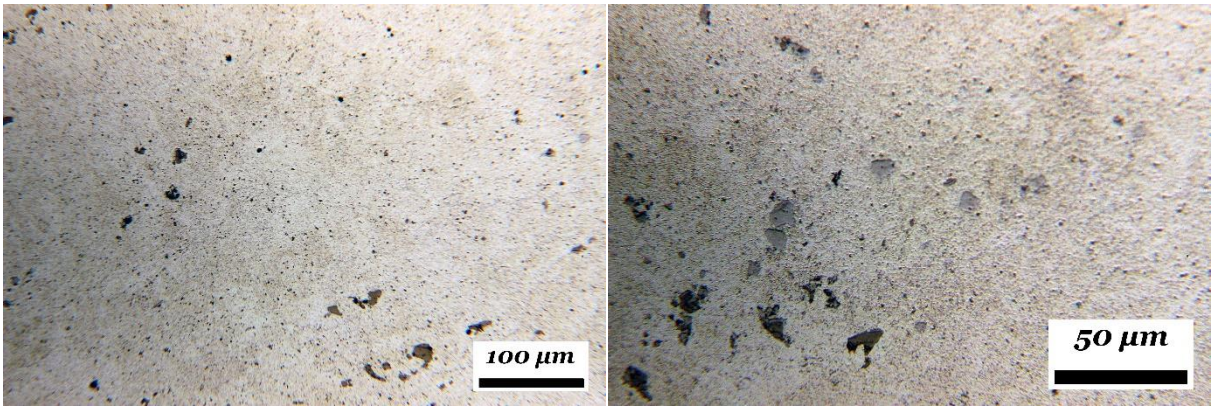

(c) **(d)**

Figure 4.6: Metallographic images from the surface of the specimens (LT plane).Images (a) and (b) depict the fracture after artificial aging at 150ºC while (c) and (d) after artificial aging at 160ºC. Magnifications used are x200 for (a)&(c) and x500 for (b)&(d). Aging time was 96 hours in all cases.

Aging time- 120 hours

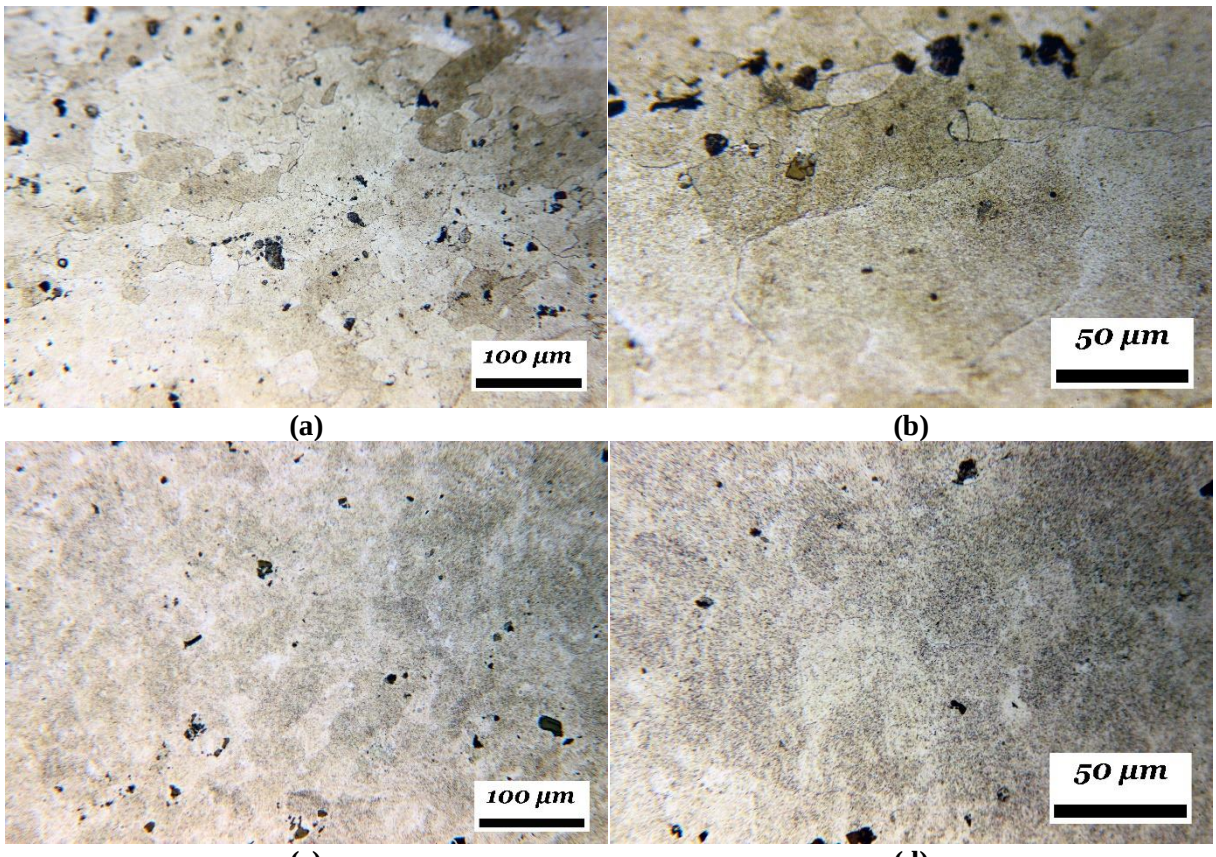

(a) **(b)**

(c) **(d)**

Figure 4.7: Metallographic images from the surface of the specimens (LT plane).Images (a) and (b) depict the fracture after artificial aging at 150ºC while (c) and (d) after artificial aging at 160ºC. Magnifications used are x200 for (a)&(c) and x500 for (b)&(d). Aging time was 120 hours in all cases.

4.2 Weight Loss measurements

Another batch of specimens was used to measure the weight loss of the alloy samples after an exposure to the EXCO environment for 24 hours. Again, the specimens were artificially aged, after solid solution at 495°C for 30 min, at 150°C and 160°C in an induction oven with ±3 °C temperature control. The aging times were: 30 min, 1h, 2h, 4h, 6h, 9h, 15h, 24h, 48h, 63h, 96h, and 120h respectively. Three weight measurements have been conducted to each specimen separately in a high accuracy weight scale with ±0.1 mg control. First sample was right after the artificial aging procedure, the second one after the 24 hours exposure and the last one after rinsing in pure HNO_3 for 5 minutes to remove any residuals. The final result was the difference between the first and the third measurement.

The weight loss study for alloy 2024 (Figure 4.8) revealed that the maximum weight loss for specimens treated at 150°C was found in 120 hours and peaked at 94.5 mg while the maximum weight loss for the one treated at 160°C was found in 96 hours and peaked at 104.1 mg. Another remarkable observation is that is both situations we found a fluctuation in small aging times followed by a sharp growth at bigger aging times.

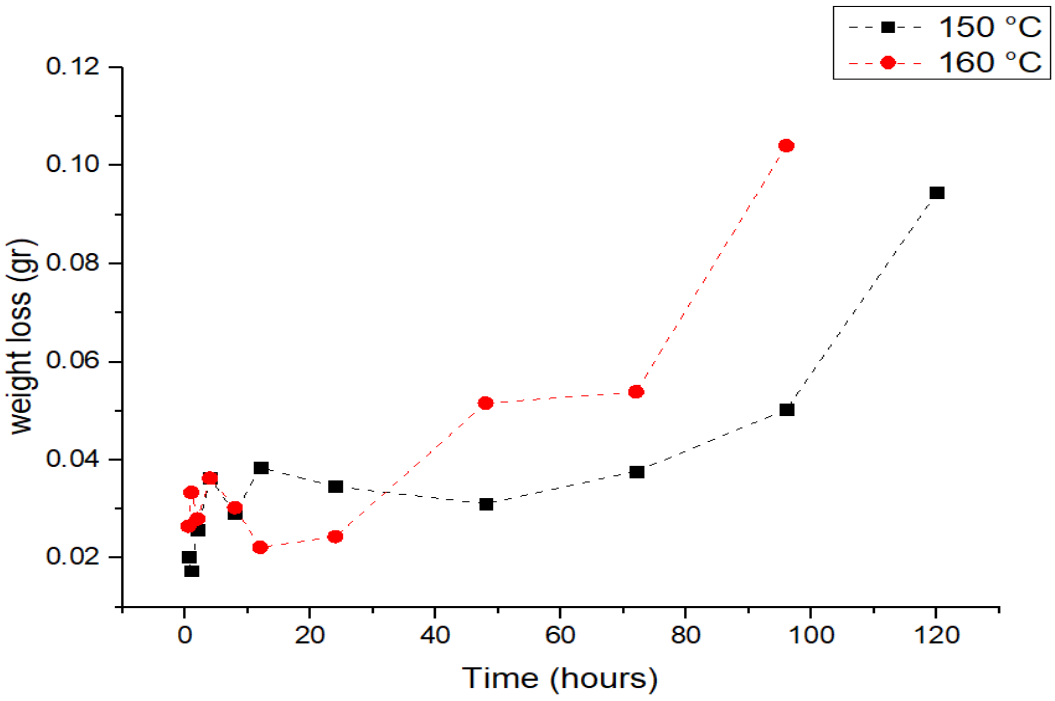

Figure 4.8**.** Weight loss samples after exfoliation corrosion testing (EXCO) was performed for 24h, for aging temperatures of 150°C and 160°C respectively.

4.3 Depth of attack

Corrosion begins in the form of isolated pits. In the first 30 minutes of exposure cavities deepen and develop laterally. The pits density increases, and the pit-to-pit interaction begins. The pits interact through intergranular corrosion. This leads to clumping of pipes and formation of a cluster of pits. The bottom agglomerates develop laterally beneath the surface of the material through intergranular corrosion. The affected boundaries run parallel to the rolling direction, leading to exfoliation of the surface layers of the material. This type of damage can be seen better for aging times exceeding 12 hours. Moreover, this type of damage evolution, meaning the intergranular network that supports the growth of the pits, is also responsible for transporting a corrosion solution deep into the material so that the corrosion reaction takes place at a certain depth producing hydrogen. This is one of the main mechanisms of hydrogen transport at relatively high depths, which otherwise cannot be explained solely by diffusion from the surface of the material. However, when hydrogen is produced, e.g. at the bottom of an erosion pit, it diffuses into the adjacent unaffected material and creates a hydrogen diffusion zone below the corrosion zone. A batch of specimens was exposed to the exfoliation solution for 24 hours after SQA for 1 to 120 hours and for temperatures of 150°C and 160 °C. Characterization of microstructure as well as depth of attack measurements were performed by means of light optical metallography (LOM) and Image Pro Plus analysis.

4.3.1 Corrosion exposure for 24 hours

Figure 4.9 (a) depicts the exfoliation in the LS plane and image Figure 4.9 (b) depicts exfoliation in the ST plane. The magnification used is x100 and the maximum depth of attack was measured at 118.5813 μm for image (a) and 188.280 μm for image (b).

1-hour aging at 150°C

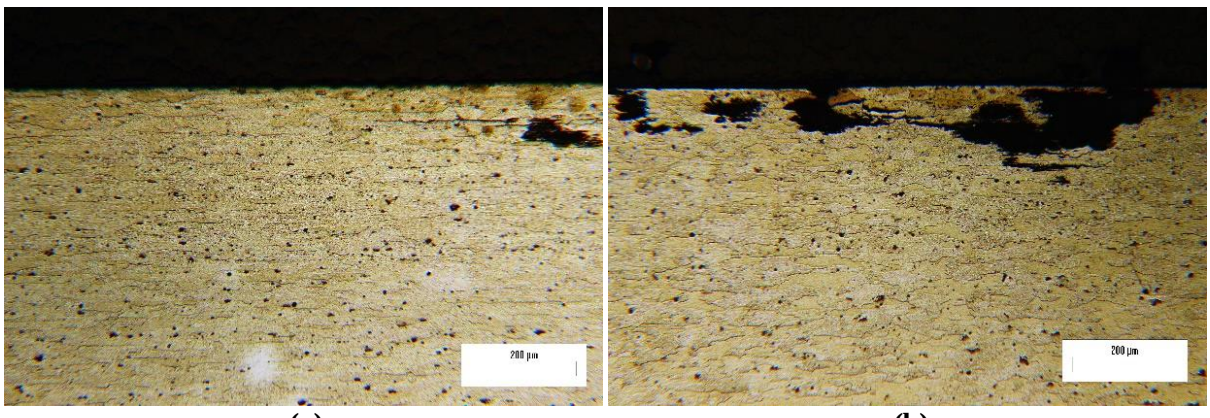

(a) **(b)**

Figure 4.9 Exfoliation corrosion for alloy 2024-T351 for aging time of 1 hour at T=150°C. (a) depicts exfoliation in the LS plane and image (b) depicts exfoliation in the ST plane. The magnification used is x100.

Image Figure 4.10 (a) depicts exfoliation in the LS plane and image (b) depicts exfoliation in the ST plane. The magnification used is x100 and the maximum depth of attack was measured at 141.5936 μm for image (a) and 113.9645 μm for image (b).

1-hour aging at 160^{o}C

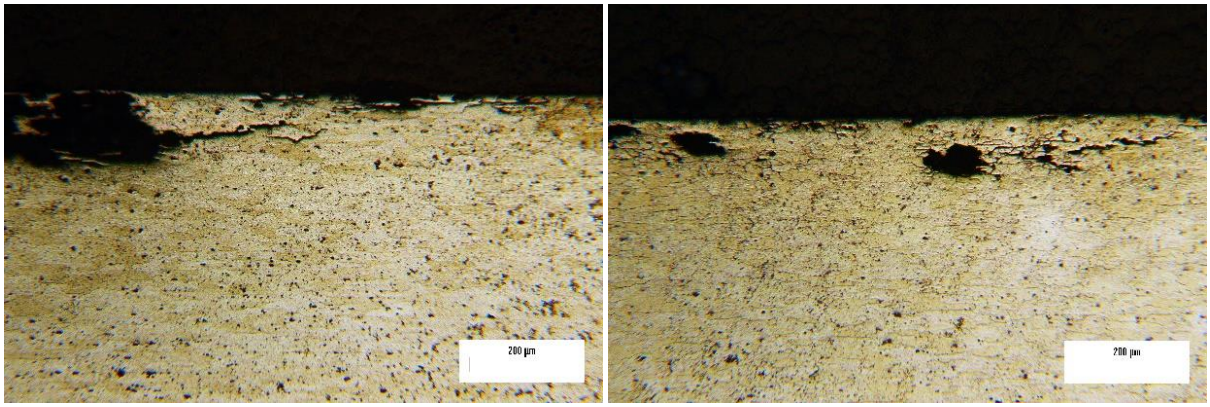

(a) **(b)**

Figure 4.10 Exfoliation corrosion for alloy 2024-T351 for aging time of 1 hour at T=160^{o}C. Image (a) depicts exfoliation in the LS plane and image (b) depicts exfoliation in the ST plane. The magnification used is x100.

Figure 4.11 (a) depicts the exfoliation corrosion for alloy 2024-T351 for aging time of 12 hours at T=150^{o}C.Image (a) depicts exfoliation in the LS plane and image (b) depicts exfoliation in the ST plane. The magnification used is x100 and the maximum depth of attack was measured at 258.0236 μm for image (a) and 316.5979 μm for image (b).

12-hour aging at 150^{o}C

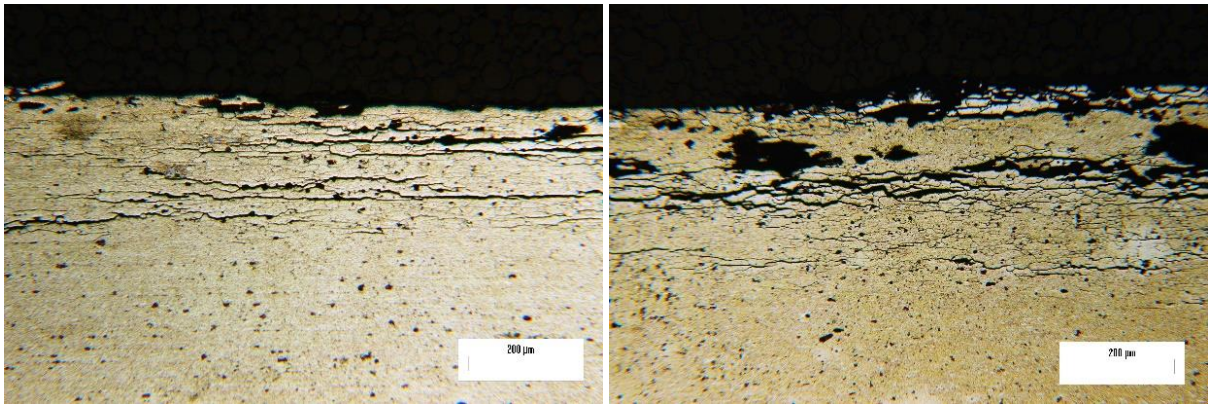

(a) **(b)**

Figure 4.11 Exfoliation corrosion for alloy 2024-T351 for aging time of 12 hours at T=150^{o}C.Image (a) depicts exfoliation in the LS plane and image (b) depicts exfoliation in the ST plane. The magnification used is x100.

Figure 4.12 depicts the exfoliation corrosion for alloy 2024-T351 for aging time of 12 hours at T=160ºC.Image (a) depicts exfoliation in the LS plane and image (b) depicts exfoliation in the ST plane. The magnification used is x100 and the maximum depth of attack was measured at 273.4438 μm for image (a) and 221.6755 μm for image (b).

12-hour aging at 160ºC

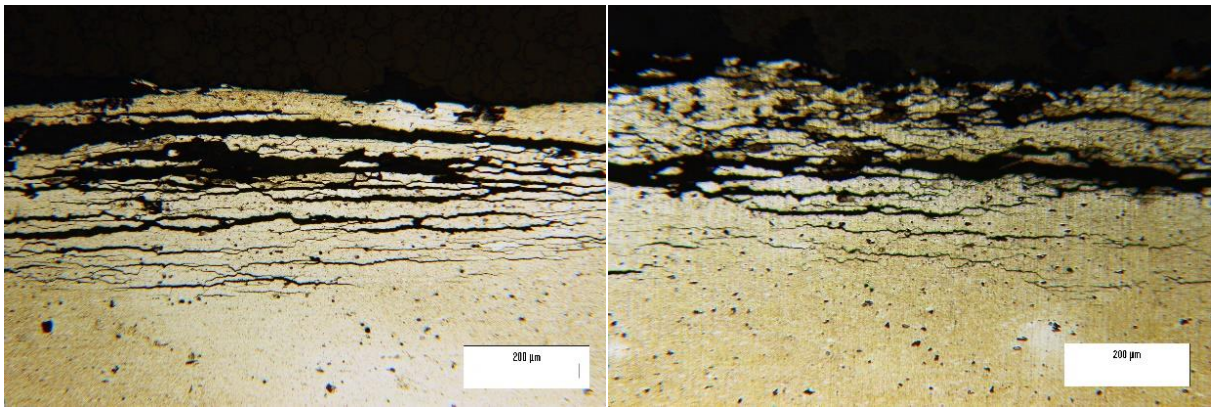

(a) **(b)**

Figure 4.12 Exfoliation corrosion for alloy 2024-T351 for aging time of 12 hours at T=160ºC.Image (a) depicts exfoliation in the LS plane and image (b) depicts exfoliation in the ST plane. The magnification used is x100 and the maximum depth of attack was measured at 273.4438 μm for image (a) and 221.6755 μm for image (b).

24-hour aging at 150ºC

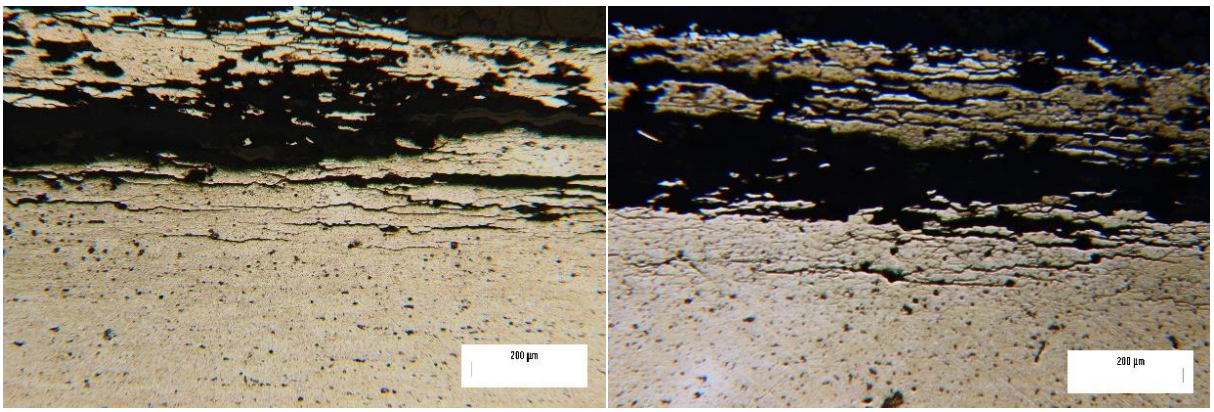

(a) **(b)**

Figure 4.13 Exfoliation corrosion for alloy 2024-T351 for aging time of 24 hours at T=150ºC.Image (a) depicts exfoliation in the LS plane and image (b) depicts exfoliation in the ST plane. The magnification used is x100 and the maximum depth of attack was measured at 192.0311 μm for image (a) and 151.1320 μm for image (b).

24-hour aging at 160°C

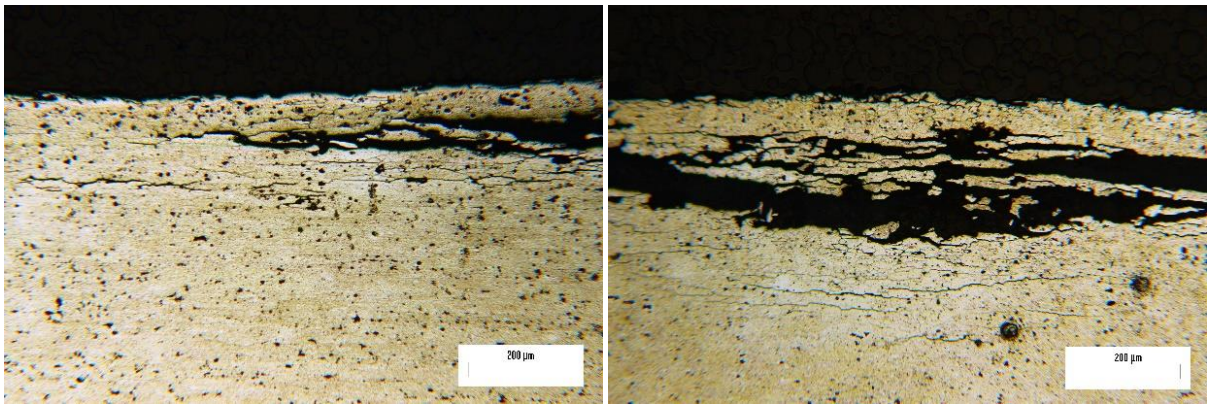

(a) **(b)**

Figure 4.14 Exfoliation corrosion for alloy 2024-T351 for aging time of 24 hours at T=160°C.Image (a) depicts exfoliation in the LS plane and image (b) depicts exfoliation in the ST plane. The magnification used is x100 and the maximum depth of attack was measured at 215.7187 μm for image (a) and 256.4083 μm for image (b).

72-hour aging at 150°C

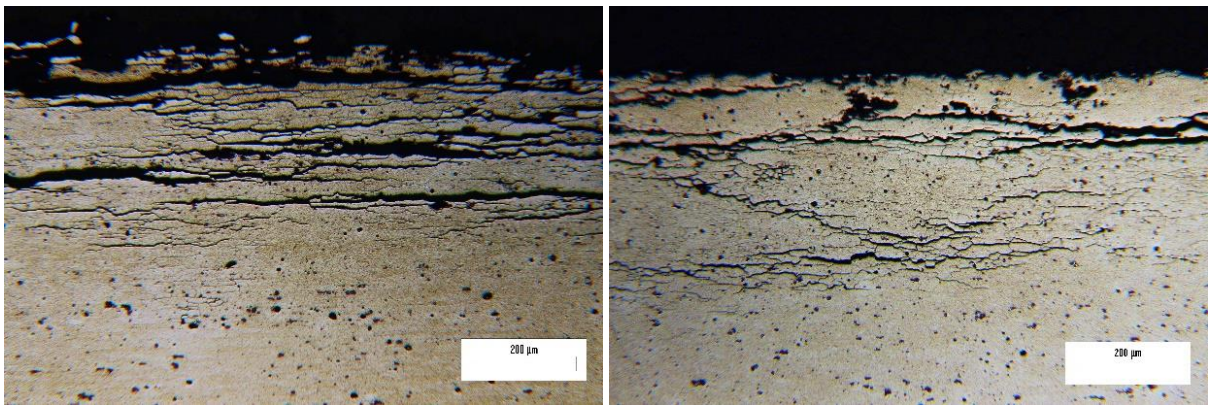

(a) **(b)**

Figure 4.15 Exfoliation corrosion for alloy 2024-T351 for aging time of 72 hours at T=150°C.Image (a) depicts exfoliation in the LS plane and image (b) depicts exfoliation in the ST plane. The magnification used is x100 and the maximum depth of attack was measured at 301.3255 μm for image (a) and 399.1024 μm for image (b).

72-hour aging at 160°C

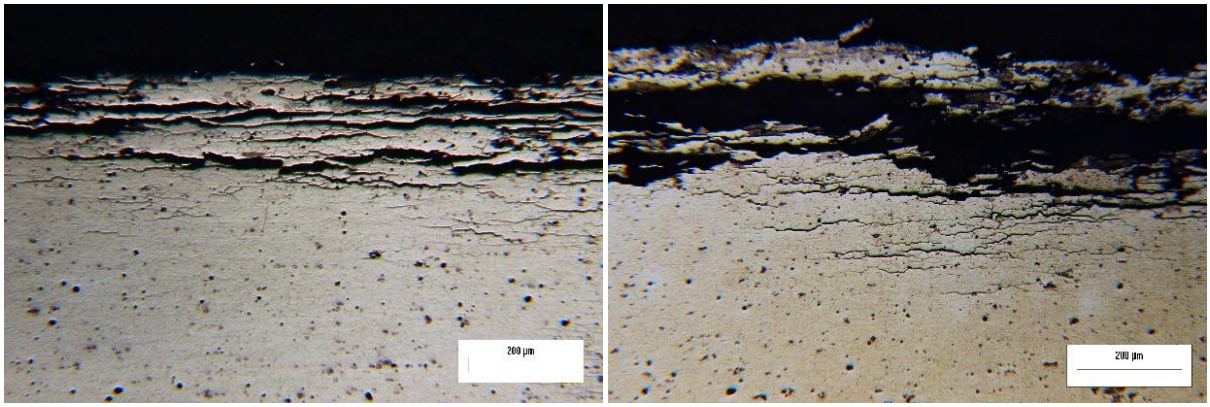

(a) **(b)**

Figure 4.16 Exfoliation corrosion for alloy 2024-T351 for aging time of 72 hours at T=160°C.Image (a) depicts exfoliation in the LS plane and image (b) depicts exfoliation in the ST plane. The magnification used is x100 and the maximum depth of attack was measured at 201.5413 μm for image (a) and 267.7252 μm for image (b).

96-hour aging at 150°C

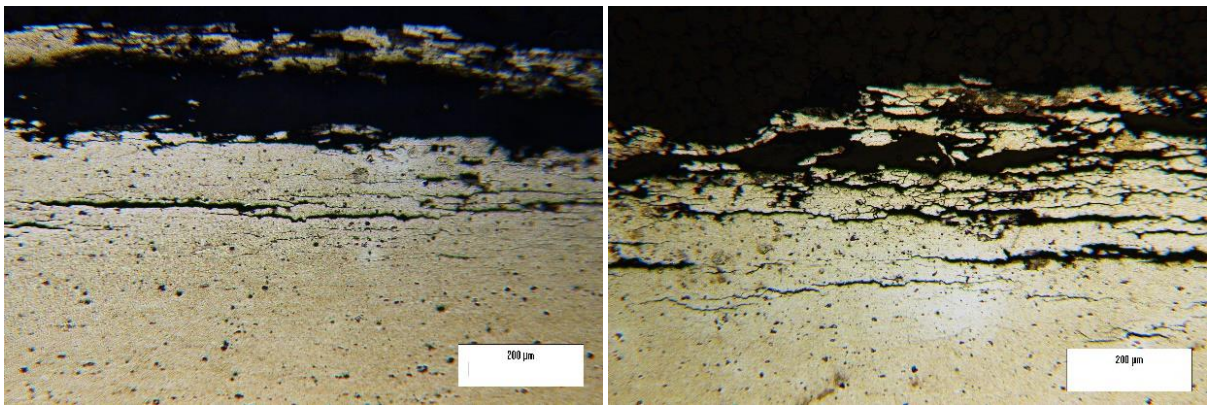

(a) **(b)**

Figure 4.17 Exfoliation corrosion for alloy 2024-T351 for aging time of 96 hours at T=150°C.Image (a) depicts exfoliation in the LS plane and image (b) depicts exfoliation in the ST plane. The magnification used is x100 and the maximum depth of attack was measured at 221.4626 μm for image (a) and 309.2819 μm for image (b).

96-hour aging at 160°C

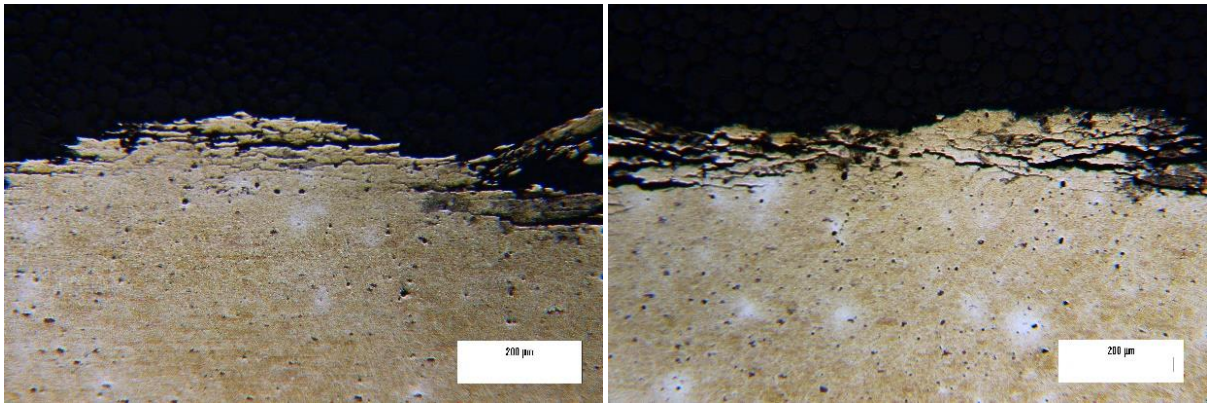

(a) **(b)**

Figure 4.18 Exfoliation corrosion for alloy 2024-T351 for aging time of 96 hours at T=160^{o}C.Image (a) depicts exfoliation in the LS plane and image (b) depicts exfoliation in the ST plane. The magnification used is x100 and the maximum depth of attack was measured at 170.1331 μm for image (a) and 168.3634 μm for image (b).

120-hour aging at 150^{o}C

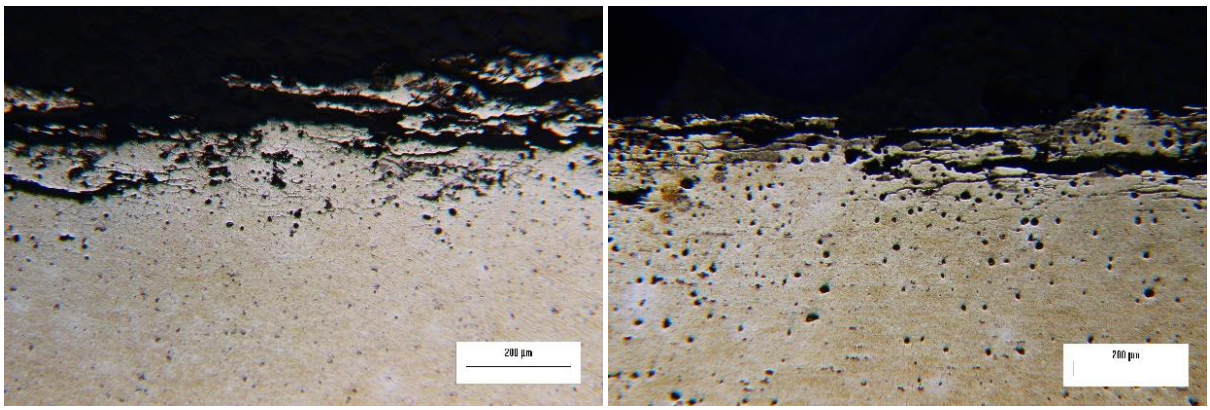

(a) **(b)**

Figure 4.19 Exfoliation corrosion for alloy 2024-T351 for aging time of 120 hours at T=150^{o}C.Image (a) depicts exfoliation in the LS plane and image (b) depicts exfoliation in the ST plane. The magnification used is x100 and the maximum depth of attack was measured at 142.6978 μm for image (a) and 122.3411 μm for image (b).

120-hour aging at 160°C

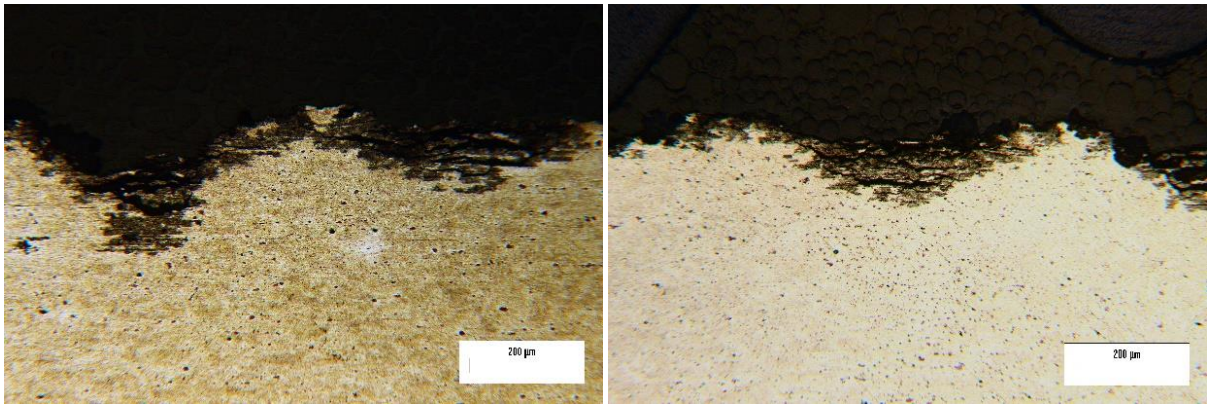

(a) **(b)**

Figure 4.20 Exfoliation corrosion for alloy 2024-T351 for aging time of 120 hours at T=160°C.Image (a) depicts exfoliation in the LS plane and image (b) depicts exfoliation in the ST plane. The magnification used is x100 and the maximum depth of attack was measured at 240.0365 μm for image (a) and 151.1043 μm for image (b).

4.4 Potentiodynamic Test

The aged aluminum specimens were subjected to potentiodynamic (PD) tests to evaluate the effect of the aging heat treatment on corrosion. Coupon-shaped specimens were placed on an epoxy resin leaving an exposed surface of $1cm^2$. They were then slightly abraded with SiC papers gradually up to 2400 grit and dried after rising. A Reference 3000 potentiostat from Gamry Instruments was used for the PD tests with a three electrode-type cell setup, a saturated calomel electrode (SCE) as the reference electrode and a graphite bar as the counter electrode. The test solution was 3.5 % NaCl with a pH about 7. The open circuit potentials (OCP) for 5 and 10 minutes were measured to check the corrosion potential of each aged Al alloy sample. The samples were cathodically treated at starting potentials of -1 ±0.03V (vs. SCE) for 5 minutes at first test and 10 minutes at second test to remove any pre-existing oxides and then polarized in the positive direction from the cathodic treatment potential at 1 mV/sec scan rate. They were polarized up to the potentials corresponding to current values of 1mA and 10mA. All the tests were performed two times with same conditions at room temperature. Again this experimental procedure leading to these raw data, was conducted and partly funded by Khalifa University, Abu Dhabi, UAE, with an internal start-up fund under the project No.847400013 on Hydrogen Embrittlement of Aluminum Alloys.

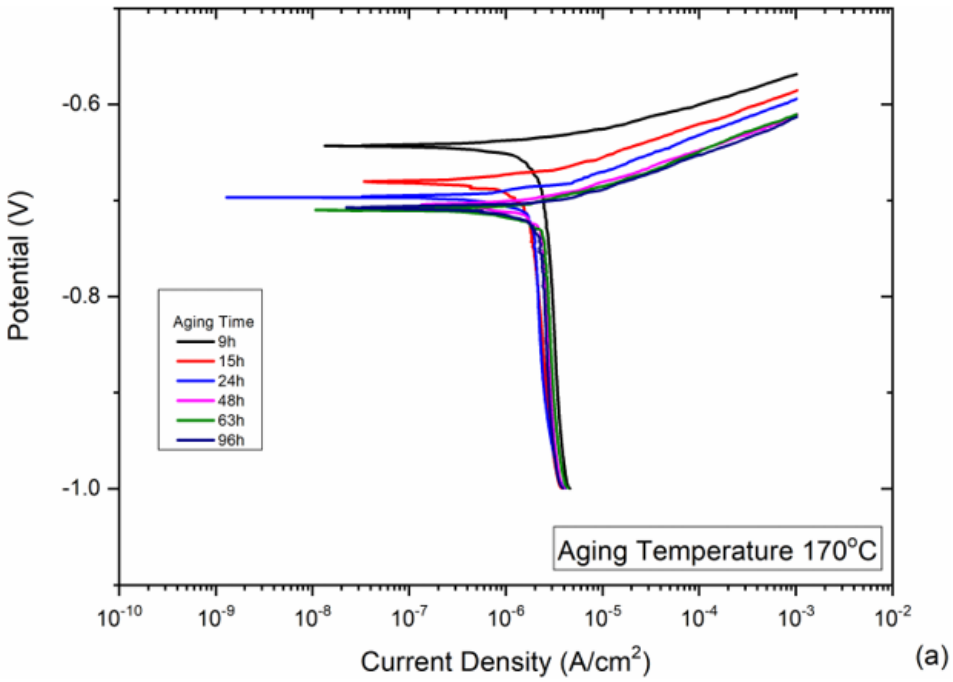

Figure 4.21: Potentiodynamic curves for different aging times for 170ºC aging temperature.

An active region after E_{corr} without passive state was observed in all aging times for both aging temperatures. The variation of corrosion potential E_{corr} vs. aging time is depicted in Figure 4.21. The corrosion potential becomes more negative. i.e. the driving force for corrosion increases with aging time. The formation of precipitates causes copper depletion from the surrounding matrix and leads to the formation of local electrochemical cells between the matrix and precipitates. With the evolution of aging, from the coherent to semicoherent and finally to incoherent precipitates, these cells become more established and corrosion damage increases [32-34].

4.5 Transmission Electron Microscopy (TEM)

Transmission electron microscopy (TEM) was also performed on samples to determine the degree of coherency of precipitates in the Al matrix. This was achieved by identifying the strain fields around the precipitates. It has been contended that the presence of strain fields due to dislocations is indicative of incoherent or semicoherent precipitates, whereas, no dislocation strain fields in the maps implies a fully coherent precipitate in Al matrix. TEM analysis of samples was carried out by utilizing an aberration-corrected microscope of model Titan 80-300 ST equipped with electron energy-loss spectroscopy (EELS) detector. The accelerating voltage of the microscope was set to 300 kV and the imaging was accomplished in TEM mode in a range of magnifications. Moreover, microstructure of samples was also determined by recording selected area electron diffraction (SAED) patterns along $[100]_{Al}$ zone axis. In the final step, the geometrical phase analysis (GPA) was applied high-resolution TEM (HRTEM) images to determine the distribution of strain fields around the precipitates. TEM specimen preparation was done by employing the dual-beam scanning electron microscope (DB-SEM) of model FIB Helios 450 from ThermoFisher Scientific. In this way, specimens of thickness about 60-80 nm in the beam-penetrating direction were prepared.This experimental procedure leading to these raw data, was conducted and partly funded by Khalifa University, Abu Dhabi, UAE, with an internal start-up fund under the project No.847400013 on Hydrogen Embrittlement of Aluminum Alloys.

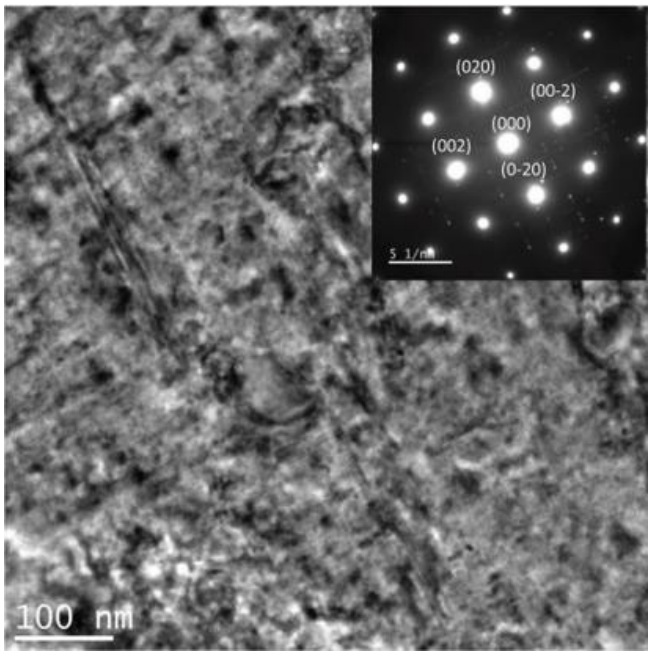

Figure 4.22: BF-TEM image along with corresponding SAEDs as insets show the microstructure of 170ºC/24h aged samples.

Figure 4.22 shows TEM micrographs along the [100] zone axis with associated diffraction patterns. The primary diffraction peaks correspond to the FCC matrix phase while secondary peaks correspond to precipitates.

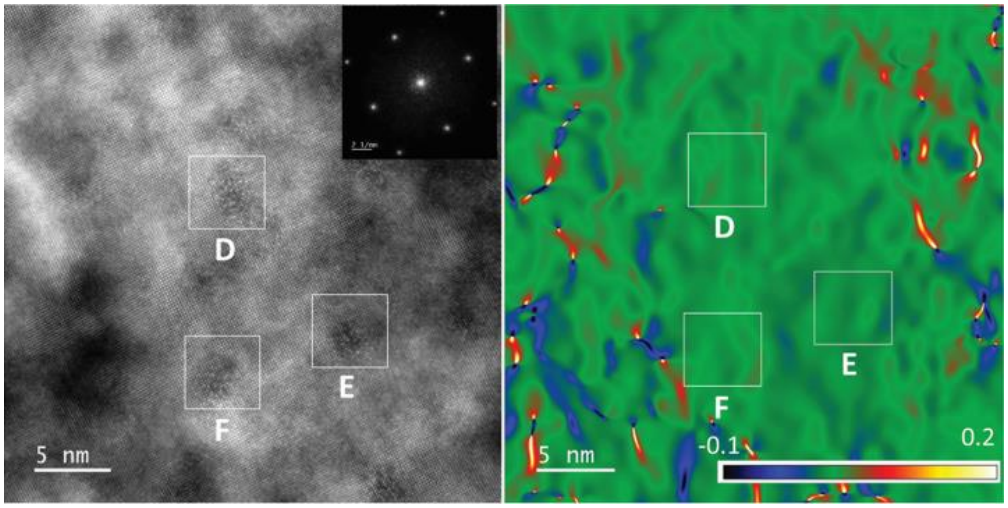

(a) **(b)**

Figure 4.23: HR-TEM image along with corresponding FFT as insets, show the microstructure of 170°C/24h aged samples followed by the corresponding GPA determined strain map on (020) planes.

The microstructure is complex and can only be revealed with high-resolution microscopy HRTEM. Representative micrographs, associated diffraction patterns and respective strain maps, obtained by geometric phase analysis (GPA) [63-67] are shown in Figure 4.23. Precipitates D, E and F (a) for the 170°C specimen are not associated with strain dipoles (dislocations) but with a high matrix strain (b) determined around end-on oriented precipitates, indicating that these precipitates are coherent GPB zones/S´´ precipitates. Trapping state T2 could, therefore, be attributed to the coherency stress fields of coherent GPB1 and GPB2/S´´ phases.

4.6 Microhardness Profile

Specimens of dimensions 5mm x 10mm^2 were cut out of an un-cladded 2024 plate. The small size and volume of the specimen was necessary for the uniform transport of heat into the sample during thermal treatment. First, the specimens were surface cleaned with alcohol according to ASTM G1 and then were heat treated. The specimens were artificially aged, after solid solution at 495°C for 30 min, at 150°C and 160°C in an induction oven with ±3 °C temperature control. The aging times were: 30 min, 1h, 2h, 4h, 6h, 9h, 15h, 24h, 48h, 63h, 96h, 120h, 168h, 216h and 264h respectively.

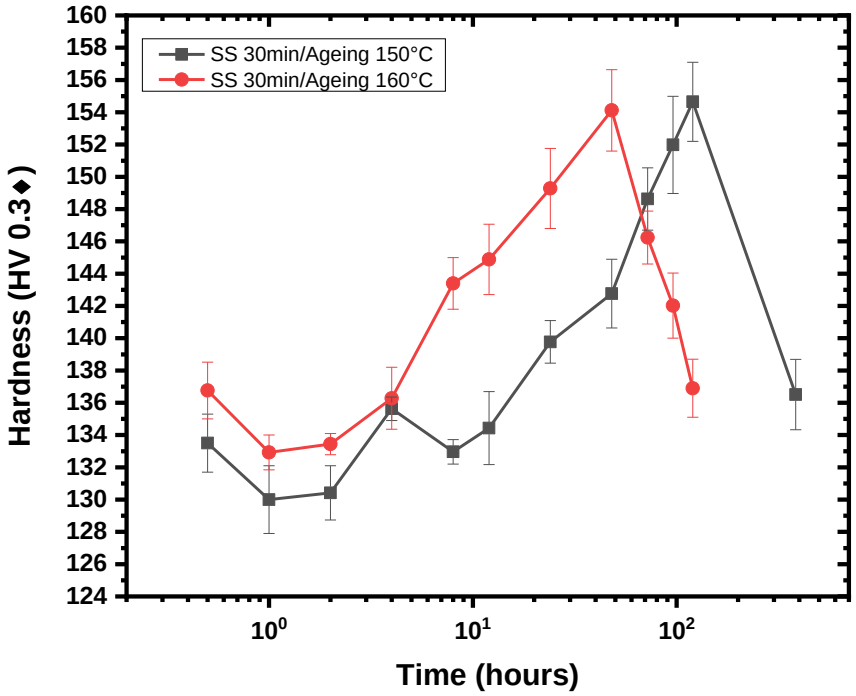

Figure 4.24: Microhardness profile of 2024-T351 versus time of aging. Aging was performed at T=150ºC and T=160ºC for duration of 30 min, 1 h, 2 h, 4 h, 8 h, 12 h, 24 h, 48 h, 72 h, 96h, 120h, 168h, 216h and 264h respectively.

The microhardness study of artificial aging for alloy 2024 (Figure 4.24) revealed that after solid solution and aging at 150ºC and 160ºC, the specimens reached the maximum microhardness of 155HV aging between 30 and 120 hours respectively and the alloy microhardness subsequently drops at longer aging times. This is attributed to the formation of coherent Cu-Mg Clusters, semi-coherent particles of GPB zones (Guinier-Preston-Bagaryatsky), S'' and S' phases that are present at small aging times. As aging time progresses the particles increase in size, thus increasing the hardness of the material due to coherency hardening and eventually reaching the S phase. The S phase is the equilibrium phase with composition $CuMgAl_2$ and exhibits an orthorhombic crystal structure and rod morphology. It is incoherent with the matrix. The S´ phase has a structure almost identical to S but it is semi coherent with the matrix and exhibits a platelet morphology. Its interfacial structure is characterized by the formation of misfit dislocations, which form in order to relieve the strain energy. After the peak, S'' is no longer present as it is gradually replaced by the semi coherent S' and at even longer times by the incoherent S phase where the interfaces loose coherency. The hardness drops and follows Orowan-mechanism. This is attributed to the coarsening of the S´ and S phases.

4.7 Spectrum of hydrogen

A major part of this work consists of determining the hydrogen concentration and trapping states in the material after corrosion. The determination of these conditions was carried out using a thermal desorption technique. The results reported in the next section are presented as the hydrogen mass flow rate (in μg / min) versus the sample temperature.

If the heating rate is sufficiently low, each trapping location produces an independent peak. The temperature of the onset of maximum growth is characteristic of the energy required to release hydrogen from the corresponding trapping site. Thus, low temperature peaks are associated with weakly bound hydrogen and high temperature peaks with strongly bound hydrogen. The calculation of the total amount of hydrogen at each trapping site is performed by integrating the area below the corresponding peak. Experiments were carried out on the hydrogen desorption of the alloy 2024-T351 after exposure to the EXCO corrosion solution 24 hours and the results are presented in the following figures. According to the previous work, four separate trapping states are observed. Hydrogen is produced during the corrosion process and is trapped in different energy states corresponding to different microstructure traps. These traps are activated and release hydrogen at different temperatures. In alloy 2024, four traps T1 to T4 were identified. The T1 trap is considered a reversible trap, which releases hydrogen continuously at low temperatures. The T2, T3 and T4 traps are saturated with exposure time and are considered irreversible.

As the aging time increases, there is an increase in the hydrogen trapped in the material. Different trapping states trap hydrogen in a different way, thus providing evidence for the microstructural characteristics associated with the respective trap. Trapping state T1 corresponds to hydrogen at interstitial sites. The observed material softening at the same temperature range of T1 activation correlates with theories of hydrogen-induced softening stemming from dislocation-hydrogen interactions. Trapping state T4 is the strongest trap and its temperature range corresponds to the dissolution of the strengthening precipitate in alloy 2024.It is confirmed that the behavior of the T2 trapping state is connected to the peak hardness of the materials. Aging temperatures 150^{o}C (Figure 4.3) and 160 ^{o}C (Figure 4.2) exhibited similar behavior in the trapping of H_2 in the T2 trapping state as in the case of 170^{o}C, which was presented in previous work [62]. Hydrogen in the T2 state is attracted to the strain fields associated with coherent and semi-coherent interfaces.

After the peak, loose cohesion interfaces and stress fields are reduced. The hardness drops and follows the Orowan mechanism. At the same time, H2 falls as soon as H2 is absorbed into the T4 state. It has been discussed in previous work that T3 is associated with dislocation. Coherent / semi-intermediate interfaces consist of discharge arrays. As the particle size increases with age, the density of post-dislocation increases with increasing H2 with aging. After the peak, the cohesion is lost, the density of post-dislocation disintegration is reduced and so the hydrogen trapping is reduced as well.

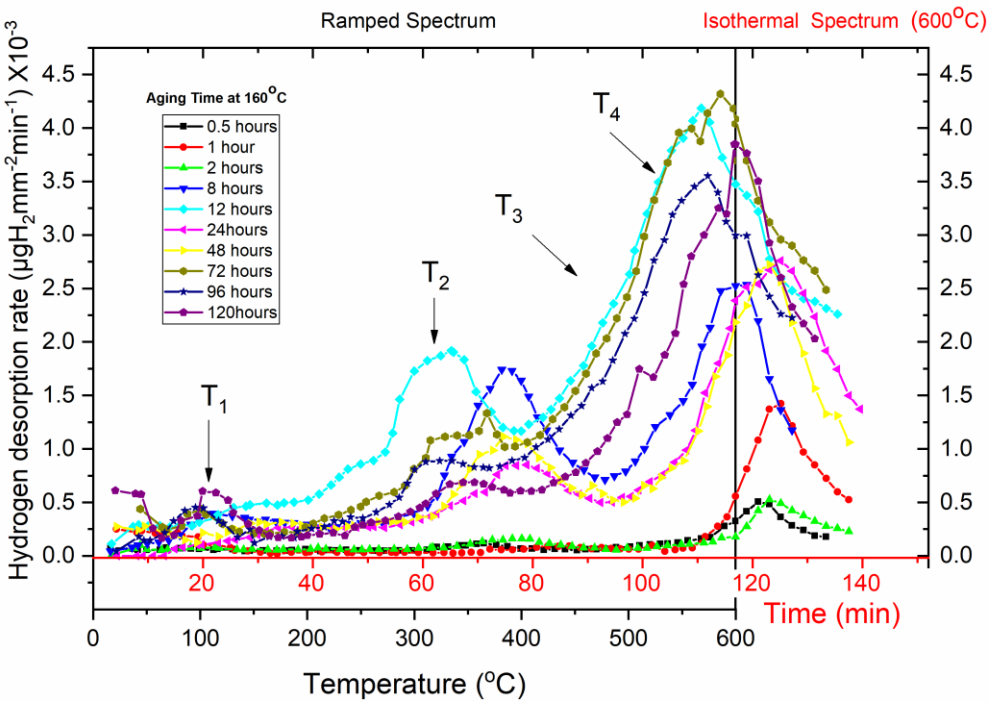

Figure 4.25: Spectrum of hydrogen evolved from the solution treated, quenched and aged specimens after 24 h in the EXCO solution. The specimens were artificially aged at T=160°C for 1 h, 24 h, 48 h, 72 h, 96h and 120h respectively.

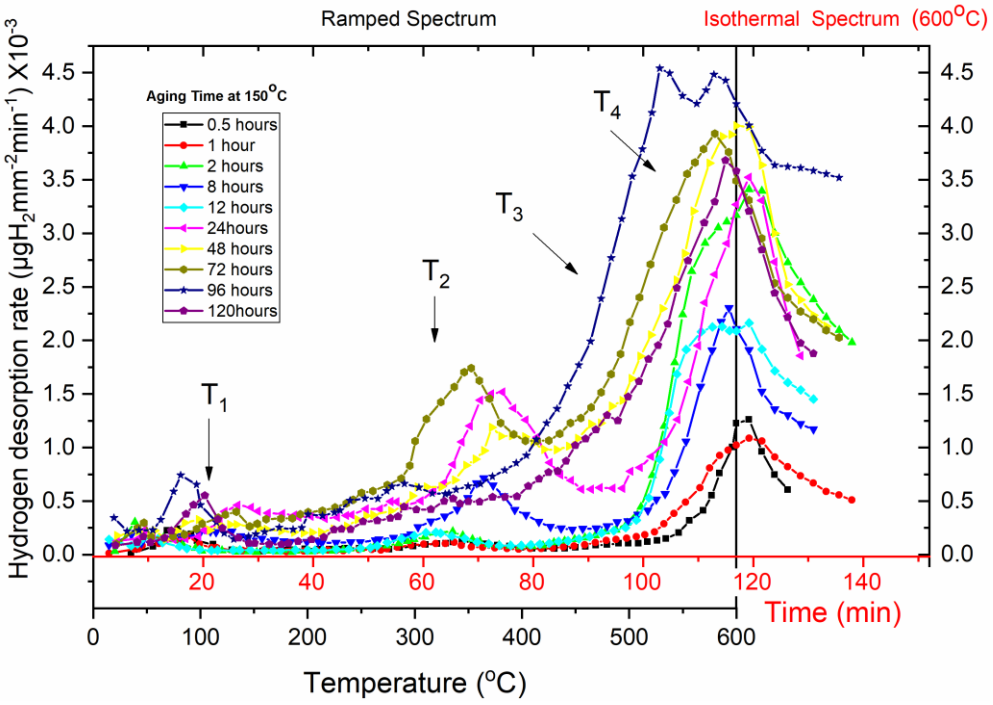

Figure 4.26: Spectrum of hydrogen evolved from the solution treated, quenched and aged specimens after 24 h in the EXCO solution. The specimens were artificially aged at T=150°C for 1 h, 24 h, 48 h, 72 h and 120h respectively.

4.8 Hydrogen trapping

Further information, regarding trapped hydrogen, can be obtained from plots of total amount of hydrogen, desorbed for each state, as a function of aging time depicted in Figure 4.27, Figure 4.28,Figure 4.29 and Figure 4.30.

T1 trapping state is shown in Figure 4.27, T2 trapping state is shown in Figure 4.28, T3 trapping state is shown in Figure 4.29 and finally the T2 trapping state is shown in Figure 4.30

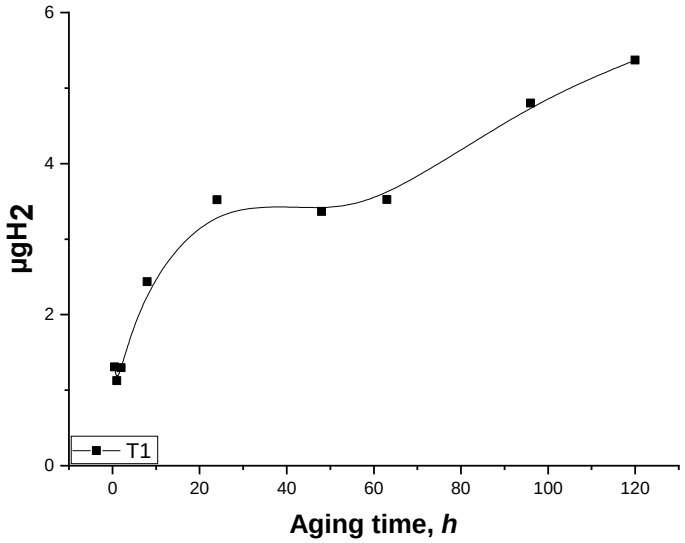

Figure 4.27: Amount of hydrogen desorbed from T1 trapping state vs. aging time for 150°C aging temperature.

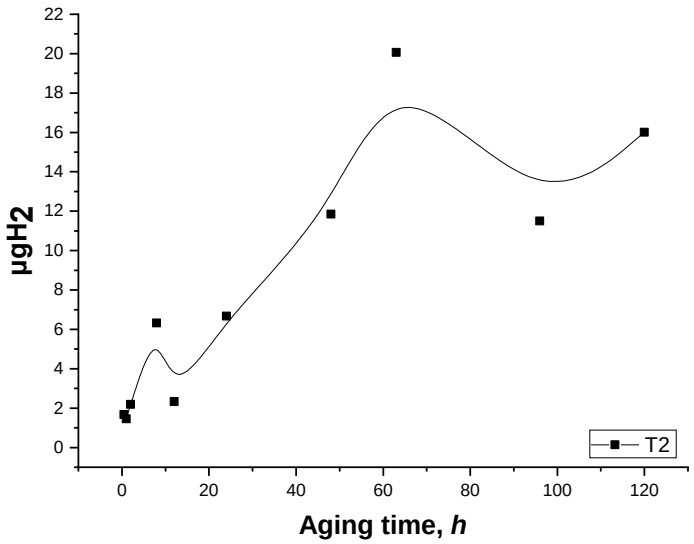

Figure 4.28: Amount of hydrogen desorbed from T2 trapping state vs. aging time for 150°C aging temperature.

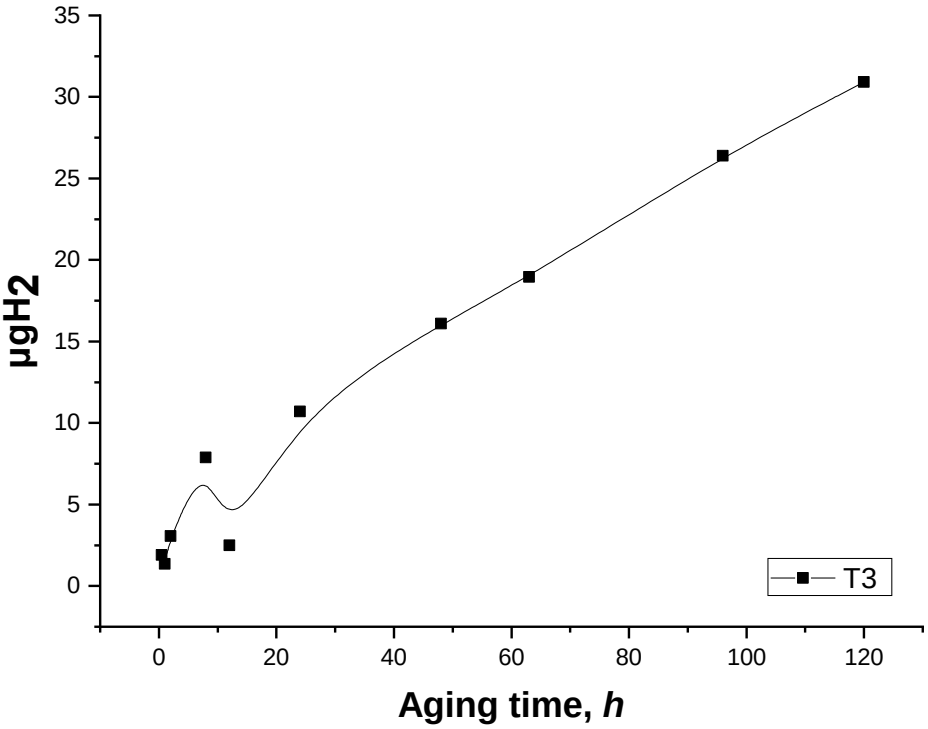

Figure 4.29: Amount of hydrogen desorbed from T3 trapping state vs. aging time for 150°C aging temperature.

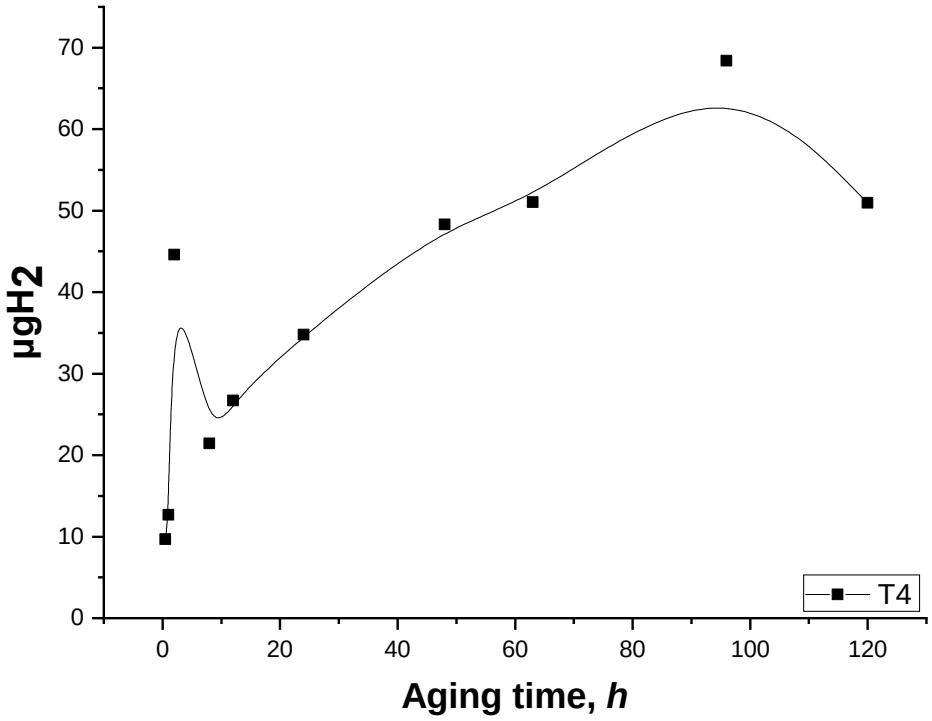

Figure 4.30: Amount of hydrogen desorbed from T4 trapping state vs. aging time for 150°C aging temperature.

Chapter 5 – Conclusions

The experiments performed in this thesis, the analysis of results and the discussion in the previous chapter led to the following conclusions regarding corrosion-induced hydrogen embrittlement in aircraft Al-alloys:

1. Corrosion damage in the alloy starts with pitting and develops to a network of intergranular corrosion leading to exfoliation of material. Pit-to-pit interaction and pit clustering are mechanisms aiding the development of corrosion damage. The depth of attack increases with exposure time. Typical value for depth of attack varies from 110mμ to 400μm for 24h of exposure time.

2. The study of artificial aging for alloy 2024 revealed that after solid solution and aging treatment at 150^{o}C and 160^{o}C respectively, the maximum peak for the mechanical properties (microhardness) of the alloy is reached after aging for 110 to 120 hours at 150^{o}C and after aging for 30 to 48 hours at 160^{o}C.

3. It is confirmed that the behavior of the T2 trapping state is connected to the peak hardness of the materials. Aging temperatures 150^{o}C and 160 ^{o}C exhibited similar behavior in the trapping of H_2 in the T2 trapping state as in the case of 170^{o}C, which was presented in previous work [62]. Hydrogen in the T2 state is attracted to the strain fields associated with coherent and semi-coherent interfaces.

4. Precipitates of the alloys after TEM observation for the 170^{o}C specimen are not associated with strain dipoles (dislocations) but with a high matrix strain determined around end-on oriented precipitates, indicating that these precipitates are coherent GPB zones/S´´ precipitates. Trapping state T2 could, therefore, be attributed to the coherency stress fields of coherent GPB1 and GPB2/S´´ phases.

Chapter 6 References

1. *AGARD Workshop*. 1998, 5-9 October. Corfu, Greece.
2. *BRITE / EURAM No. 1053*. in *ICAF '99 Conference*. 1999. Bellevue, WA.
3. FAA-NASA. 1996. Atlanta, Georgia: National Technical Information Service, Springfield.
4. Chang, J.B., M. Szamossi, and K.W. Lin, *Methods and Models for Predicting Fatigue Crack Growth under Random Loading*, in *ASTM STP 748*, ASTM, Editor. 1981: Philadelphia. p. 115.
5. Zhang, X., A.S.L. Chan, and G.A.O. Davis, Eng. Mech., 1992. **42**: p. 305.
6. Sih, G.C. and D.Y. Jeong, *Fatigue load sequence effect ranked by critical available energy density.* J. Theor. Appl. Fract. Mech, 1990. **14**: p. 141-151.
7. Pantelakis, S.G., A.T. Kermanidis, and P.G. Daglaras, *Crack-growth analysis code for assessing fatigue life of 2219-T851 aluminum specimens under aircraft structure service spectra.* J. Theor. Appl. Fract. Mech., 1997. **28**: p. 1-12.
8. Speidel, M.O., *Hydrogen embrittlement and stress corrosion cracking of aluminum alloys*, in *Hydrogen Embrittlement and Stress Corrosion Cracking*, R. Gibala and R.F. Heheman, Editors. 1992, ASM: Materials Park, OH,. p. 271-296.
9. de Jong, H.F., *Influence of environmental and temperature on the stress corrosion crack growth rate of aluminum 7075.* Aluminum, 1982. **58**: p. 526-531.
10. Inman, M.E., et al. in *FAA-NASA Symposium on the Continued Airworthiness of Aircraft Structures*. 1996. Atlanta, Georgia: National Technical Information Service, Springfield, Virginia.
11. Pantelakis, S.G., N.I. Vassilas, and P.G. Daglaras, *Effect of corrosive environment on the mechanical behavior of the advanced Al-Li alloys 2091 and 8090 and the conventional aerospace alloy 2024.* METAL, 1993. **47**: p. 135-141.
12. Pantelakis, S.G., P.G. Daglaras, and C.A. Apostolopoulos, *Tensile and energy density properties of 2024, 6013, 8090 and 2091 aircraft aluminum alloy after corrosion exposure.* J. Theor. Appl. Mech., 2000. **33**: p. 117-134.
13. Kamoutsi, H., et al., *Corrosion-induced hydrogen embrittlement in aluminum alloy 2024.* Corrosion Science, 2006. **48**(5): p. 1209-1224.
14. Kamoutsi, H., et al., *Hydrogen Trapping: Deformation and Heat Treatment Effects in 2024 Alloy*. 2006: p. 1293-1294.
15. Kamoutsi, H., et al., *Effect of prior deformation and heat treatment on the corrosion-induced hydrogen trapping in aluminium alloy 2024.* Corrosion Science, 2014. **80**: p. 139-142.
16. *<Handbook of Aluminum_ Vol. 1_ Physical Metallurocesses - George E. Totten & D. Scott MacKenzie.pdf>*.
17. Ghali, E., *Corrosion resistance of aluminum and magnesium alloys : understanding, performance, and testing*. Wiley series in corrosion. 2010, Hoboken, N.J.: John Wiley. xxi, 719 p.
18. Blanc, C., B. Lavelle, and G. Mankowski, *The role of precipitates enriched with copper on the susceptibility to pitting corrosion of the 2024 aluminium alloy.* Corrosion Science, 1997. **39**(3): p. 495-510.
19. Guillaumin, V. and G. Mankowski, *Localized corrosion of 2024 T351 aluminium alloy in chloride media.* Corrosion Science, 1999. **41**: p. 421-438.
20. Liao, C.-M., et al., *In-situ monitoring of pitting corrosion in aluminum alloy 2024.* Corrosion, 1998. **54**(6): p. 451-458.
21. ASM, *Corrosion of Aluminum and Aluminum Alloys*, ed. J.R. Davis. 1999.
22. Tanguy, D., et al., *Hydrogen effects during IGSCC of pure Al-5Mg alloy in NaCl media.* Corrosion Science, 2002. **44**: p. 1163-1175.
23. Delafosse, D. and T. Magnin, *Hydrogen induced plasticity in stress corrosion cracking of engineering systems.* Eng. Fract. Mech, 2001. **68**: p. 693-729.
24. Braun, R., *Comparison of accelerated SCC tests performed on the aluminium alloy 2014-T651.* Werkstoffe und Korrosion, 1992. **43**: p. 453-458.
25. Braun, R., *Investigation of the SCC Behaviour of alloy 2024 using the slow strain rate technique.* Werkstoffe und Korrosion, 1993. **44**: p. 73-82.

26. Braun, R., *Slow strain rate testing of high-strength aluminium alloy plate in an aqueous solution of 3% NaCl +0.3% H 2 O 2.* Werkstoffe und Korrosion, 1994. **45**: p. 369-377.
27. Braun, R. in *Aluminium Alloys- Their physical and mechanical properties*. 1994. Atlanta.
28. Braun, R., *Slow strain rate testing of aluminum alloy 7050 in different tempers using various synthetic enviroments.* Corrosion, 1997. **53**(6): p. 467-474.
29. Braun, R., *Exfoliation corrosion testing of aluminium alloys.* British Corrosion Journal, 1995. **30**(3).
30. Braun, R. 1994. Seville, Spain.
31. *ASTM G34-90*, in *Annual Book of ASTM Standards*, ASTM, Editor. 1994. p. 129.
32. Al-Anezi, M.A., G.S. Frankel, and A.K. Agrawal, *Susceptibility of conventional pressure vessel steel to hydrogen-induced cracking and stress oriented hydrogen-induced cracking in hydrogen sulfide-containing diglycolamine solutions.* Corrosion, 1999. **55**(11): p. 1101-1109.
33. Sofronis, P. and I.M. Robertson, *Atomistic scale experimental observations and micromechanical/continuum models for the effect of hydrgen on the mechanical behavior of metals*. 2001.
34. Robertson, I.M., *The effect of hydrogen on dislocation dynamics.* Eng. Fract. Mech, 2001. **68**: p. 671-692.
35. Sofronis, P., et al., *Recent Advances in the study of hydrogen embrittlement at the University of Illinois*. 2001.
36. Luu, W.C. and J.K. Wu, *Hydrogen transport and enviromental embrittlement effects in iron aluminades.* Journal of Materials Science, 2000. **35**: p. 4121-4127.
37. Luu, W.C., H.S. Kuo, and J.K. Wu, *Hydrogen permeation through nickel-plated steels.* Corrosion Science, 1997. **39**(6): p. 1051-1059.
38. Young, G.A. and J.R. Scully, *Evidence that carbide precipitation produces hydrogen traps in Ni-17Cr-8Fe alloys.* Scripta Materialia, 1997. **36**(6): p. 713-719.
39. Au, M.U., *A visible technology for display of hydrogen distribution in metals.* Journal of Alloys and Compounds, 1999. **293-295**: p. 317-323.
40. Pressouyre, G.M., *A classification of hydrogen traps in steel.* Materials transactions A, 1979. **10A**: p. 1571-1573.
41. Pressouyre, G.M., *Trap theory of hydrogen embrittlement.* Acta Metallurgica, 1979. **28**: p. 895-911.
42. McMahon Jr., C.J., *Hydrogen -induced intergranular fracture of steels.* Eng. Fract. Mech, 2001. **68**: p. 773-788.
43. Birnbaum, H.K., et al., *Hydrogen in aluminum.* Journal of Alloys and Compounds, 1997. **253-254**: p. 260-264.
44. Christodoulou, L. and H.M. Flower, *Hydrogen embrittlement and trapping in Al-6%-Zn-3%-Mg.* Acta Metallurgica, 1980. **28**: p. 481-487.
45. Pantelakis, S.G., et al. *The Effect of Existing Corrosion on the Structural Integrity of Aging Aircraft*. in *Fatigue in the Presence of Corrosion*. 1998. Corfu, Greece: AGARD Workshop.
46. Kermanidis, A.T., *Åðßäñáóç ôçò äéÜâñùóçò óôçí äïìéêÞ áêåñáéüôçôá åëáöñþí êáôáóêåõþí áðü êñÜìá áëïõìéíßïõ*, in *Department of Mechanichal Engineering and Aeronautics*. 2003, University of Patras: Greece.
47. Scamans, G.M., R. Alani, and P.R. Swann, *Pre-exposure embrittlement and stress failure in Al-Zn-Mg alloys.* Corrosion Science, 1976. **16**: p. 443-459.
48. Scamans, G.M. and C.D.S. Tuck. in *Environment- sensitive fracture of engineering materials*. 1979. New York, NY: Metallurgical Sociaty AIME.
49. Speidel, M.O., *Hydrogen embrittlement and stress corrosion cracking of aluminum alloys*. 1974.
50. Itoh, G., K. Koyama, and M. Kanno, *Evidence for the transport of impurity hydrogen with gliding dislocation in aluminum.* Scripta Materialia, 1996. **35**(6): p. 695-698.
51. Saitoh, H., Y. Iijima, and K. Hirano, *Behaviour of hydrogen in pure aluminium Al-4 mass% Cu and Al-1 mass% Mg_2Si alloys studied by tritium electron microautoradiography.* Journal of Materials Science, 1994. **29**: p. 5739-5744.
52. Young, G.A. and J.R. Scully, *The diffusion and trapping of hydrogen in high purity aluminium.* Acta Materialia, 1998. **46**(18): p. 6337-6349.

53. Tuck, C.D.S. in *On the effects of hydrogen on the behaviour of materials*. 1980. Wyoming.
54. Song, R.G., et al., *Grain boundary segregation and hydrogen-induced fracture in 7050 aluminium alloy.* Acta mater., 1995. **44**(8): p. 3241-3248.
55. Jang, W., S. Kim, and K. Shin, *Hydrogen-assisted deformation and fracture behaviors of Al 8090.* Metallurgical and Materials Transactions A, 2002. **33A**: p. 1755-1763.
56. Jang, W. and S. Kim, *Hydrogen-assisted fracture of Al 8090.* Journal of Materials Science Letters, 2000. **19**: p. 447-450.
57. Lee, S.-M. and J.-Y. Lee, *The trapping and transport phenomena of hydrogen in nickel.* Metallurgical Transactions A, 1986. **17A**: p. 181-187.
58. Haidemenopoulos, G.N., et al., *Hydrogen absorption into aluminium alloy 2024-T3 during exfoliation and alternate immersion testing.* Corrosion, 1998. **54**(1): p. 73-78.
59. EPETII/30, *Damage tolerance behavior of corroded aluminum structures*. 1999, General Secretariat for Research and Technology: Greece.
60. Scherer, J., et al., *Initial stages of the anodic etching of aluminium foils studied by atomic force microscopy.* Corrosion Science, 1999. **41**: p. 35-55.
61. Alexopoulos, N.D., et al., *The effect of artificial ageing heat treatments on the corrosion-induced hydrogen embrittlement of 2024 (Al–Cu) aluminium alloy.* Corrosion Science, 2016. **102**: p. 413-424.
62. Floratos, P., H. Kamoutsi, and G. Haidemenopoulos. *Effect of aging treatment on the corrosion-induced hydrogen trapping in AA2024*. in *5th Panhellenic Conference on Metallic Materials*. 2016. Giannena, Greece.
63. Hÿtch, M.J., E. Snoeck, and R. Kilaas, *Quantitative measurement of displacement and strain fields from HREM micrographs.* Ultramicroscopy, 1998. **74**(3): p. 131-146.
64. Hÿtch, M.J., J.-L. Putaux, and J.-M. Pénisson, *Measurement of the displacement field of dislocations to 0.03 Å by electron microscopy.* Nature, 2003. **423**(6937): p. 270-273.
65. Johnson, C.L., M.J. Hÿtch, and P.R. Buseck, *Nanoscale waviness of low-angle grain boundaries.* 2004. **101**(52): p. 17936-17939.
66. Lafouresse, M.C., et al., *Hydrogen mapping in an aluminum alloy using an alternating current scanning electrochemical microscope (AC-SECM).* Electrochemistry Communications, 2017. **80**: p. 29-32.
67. Lafouresse, M.C., et al., *A Kelvin probe force microscopy study of hydrogen insertion and desorption into 2024 aluminum alloy.* Journal of Alloys and Compounds, 2017. **722**: p. 760-766.